CHARACTERIZATION OF NANO-ENVIRONMENTS BY HYPERVELOCITY PROJECTILE SECONDARY ION MASS SPECTROMETRY

A Dissertation

by

AARON BRYANT CLUBB

Submitted to the Office of Graduate and Professional Studies of
Texas A & M University
in partial fulfillment of the requirements for the degree of

DOCTOR OF PHILOSOPHY

Chair of Committee,	Emile Schweikert
Committee Members,	David Russell
	Sarbajit Banerjee
	Robert Burghardt
Head of Department,	Simon North

May 2017

Major Subject: Chemistry

ABSTRACT

The purpose of this study was to explore the perfomance of a secondary ion mass spectrometry (SIMS) technique for probing nanovolumes. The variant of SIMS used involves bombardment with individual massive projectiles (Au_{400} and C_{60}) at $\sim$ 1 keV/atom energy coupled with separate recording of the ionized ejecta from each projectile impact. Under these conditions of event-by-event bombardment/detection, each projectile acts as a nanoprobe and secondary ion emission is from an area of 10-15 nm in diameter and a depth of up to 10 nm. The data from $\sim 1x10^6$ impacts can be searched for a specific ion or ions and their coemitted species, revealing the molecular environment around a selected moiety.

The methodology was applied to study the coverage of surfactant coatings on gold nanorods. The presented study adds a new instrumental technique for the determination of nanoparticle coverage to this discussion. While nanorod surface density is $\sim 50\%$, the analysis shows that solvent washing of the nanorods does not result in the removal of the surfactant coating where coverage remains at $\sim 90\%$. SIMS in the event-by-event bombardment/detection mode displays its promise as an analytical technique due to ease of sample preparation and drastically reduced sample requirements.

The ability to probe chemical homogeneity at the nano level allows for the characterization of the chemical environment around nanoparticles. Ultra-small gold nanoparticles, with only 55 to 225 atoms, were encapsulated in a dendrimer structure and analyzed. The comparison of mass spectra of these samples shows that the secondary ion yield of Au moieties vary linearly with the number of Au atoms. Preferential colocation of the nanoparticles and undamaged dendrimer structure was

observed, while reductively damaged dendrimer branches are shown be segregated from the nanoparticles. The preference of colocation opens new possibilities for the directed growth of gold nanoparticles within a support structure.

The interaction of carbon delivered by hypervelocity projectiles and impacted surfaces was also studied as an analogue to micrometeorite impacts. First, the difference between crystalline and condensed film samples were investigated, determining that secondary ion emission from pressed powders is enhanced over samples produced through vapor deposition. The bombardment with isotopically labeled $^{13}C_{60}$ on inorganic powders enabled the study of recombination products. Here, recombination CN and CNO ions are produced but only CN shows increasing production with higher impact velocities.

The study of the interaction of hypervelocity nanoparticles with a 2D material and ultra-thin targets (single layer graphene, multi-layer graphene, and amorphous carbon foils) has been performed using Au_{400}^{4+}. The ejected area is much larger ($\sim$60 nm^2) than that predicted by molecular dynamic simulations and a large ionization rate ($\sim$1%) is observed. The interaction proceeds in an entirely different manner for the process in 3D materials. The experimental observations indicate at least four different emission processes for the observed secondary ions: direct interaction with the projectile which produces high kinetic energy secondary ions in the transmission direction; emission of high velocity secondary ions from the rim of the rupture; emission of H_n^+ and C^+ due to a high charge around the rupture; and emission of low velocity carbon clusters due to a propagation of tears and defects in the graphene foil.

NOMENCLATURE

SIMS	Secondary Ion Mass Spectrometry
SI	Secondary Ion
LMIS	Liquid Metal Ion Source
ToF	Time of Flight
MCP	Microchannel Plate
CFD	Constant Fraction Discriminator
NIM	Nuclear Instrumentation Module
TDC	Time to Digital Converter
SAMPI	Surface Analysis and Mapping of Projectile Impacts
NR	Nanorod
CTAB	Cetyltrimethylammonium Bromide
DEN	Dendrimer
PAMAM	Poly(amido amine)
FWHM	Full Width at Half Maximum
TEM	Transmission Electron Microscopy
SEM	Scanning Electron Microscopy
SRIM	Stopping Range in Matter
TRIM	Transport of Ions in Matter

CONTRIBUTORS AND FUNDING SOURCES

TABLE OF CONTENTS

Page

LIST OF FIGURES

LIST OF TABLES

1. INTRODUCTION

Secondary ion mass spectrometry (SIMS) is an analytical technique for the analysis of a surface and provides chemical and molecular information. As all chemistry occurs at an interface, the surfaces of solids is of extreme interest to many fields beyond chemistry, such as materials engineering and catalysis. As such, many techniques have been developed in order to probe surfaces to study topology, chemical composition, surface energy, etc. SIMS has been developed into an important tool for the analysis of surfaces as it allows chemical characterization by collection of sputtered ions generated by bombardment with primary ions. These sputtered ions give insight into the chemical makeup of the surface after analysis with a coupled mass spectrometer. This introductory chapter lays a foundation of the SIMS methodology and introduces the motivation for the investigations presented throughout this dissertation. The recurring theme for all studies is the desire to probe nanoenviroments in order to elucidate the chemical composition of a surface and understand the interactions between the bombarding projectile-surface or neighboring sample components to give insight into chemical processes.

An overview of SIMS is provided in order to acquaint the reader with fundamental features of the technique. Cluster bombardment and static SIMS are introduced so that an understanding of our event-by-event bombardment and detection scheme can be made. Coincidence analysis allows for the collection of chemical information from discrete nanoenviroments to calculate coverage and probe nanodomains.

SIMS analysis is predicated on the use of energetic primary ions to cause sputtering of a surface of interest. In each impact secondary ions, electrons, and photons are emitted and can be collected where the secondary ions can be analyzed by mass

spectrometry. The sputtering volume is defendant on the primary projectile and the physical properties of the analyte surface, but can be generally classified as a nanoscopic probing technique where each individual projectile has a volume of ion emission diameter of a few tens of nanometers or less (Figure 1.1).

1.1   Dynamic vs Static SIMS

Two major branches of SIMS exist and are classified based on the degree of damage done to the sample surface. For trace analysis, it is desirable to sputter as much sample as possible in order to increase the volume analyzed. At sufficiently larger sample volumes, elemental detection limits in the parts per billion are achievable. It is also possible to perform analysis into the sample depths through the removal of the topmost levels, making it possible to chart the changing chemical concentrations as a function of depth within a sample. Understandably, operating in either of these analysis modes causes destruction of the sample and falls under the category of dynamic SIMS[1]. Static SIMS, by comparison, is a relatively non-destructive technique as surface damage is greatly reduced ($< 1\%$). Static SIMS limits the dose of the primary ion to less than 10^{23} primary ion impacts/cm^2 which reduces the probability that a specific impact site will be rebombarded during the analysis[2]. This ensures that all collected secondary ions are from impacts on pristine sample, preserving information about the chemical environment. As a drawback, static SIMS limits the ultimate sensitivity which makes it desirable for the use of projectiles that are efficient in producing secondary ions (SIs) in order to populate a mass spectrum with useful ion peaks.

1.2   Cluster Projectiles

The need for cluster projectiles as the bombarding primary ions arises from the desire to have a high secondary ion yield, i.e., maximizing the number of secondary
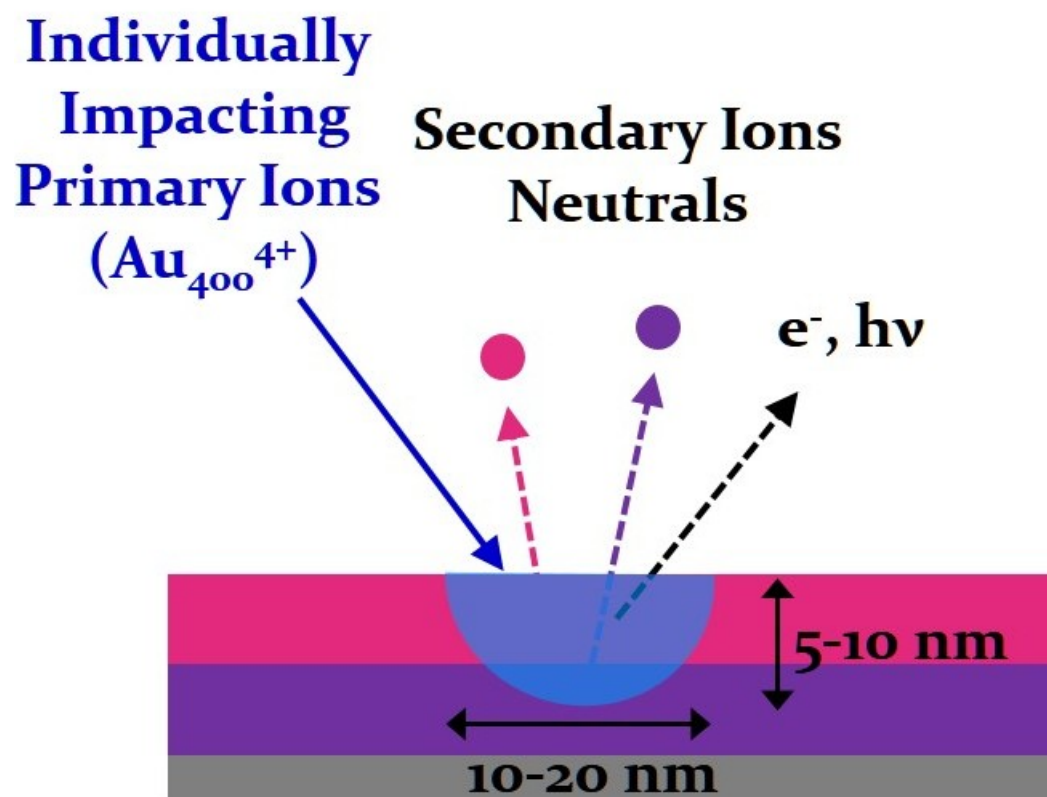
Figure 1.1: SIMS Bombardment and Emission

ions emitted from each individual impact. Atomic beams were utilized extensively in early SIMS studies given the ease of production of sources and of focusing the resultant beams[3]. It is possible to increase the SI yield by increasing the impact energy of the projectile, however once the kinetic energy exceeds 100-150 keV a plateau appears[4, 5].

The first observations of the effectiveness of clusters date to 1960, when diatomic and triatomic projectiles were observed to have an enhanced sputter yield over that of an atomic projectile with equal velocity[6, 7]. This enhancement factor[8], K_n, is defined as

$$K_n = \frac{Y_{A_n}(E)}{nY_A(\frac{E}{n})} \tag{1.1}$$

Where $Y_{An}(E)$ is the yield of ions using a cluster (A_n) to bombard with a kinetic energy of (E), and $Y_n(\frac{E}{n})$ is the yield of ions using an atomic projectile (A) with a kinetic energy of $\frac{E}{n}$. When K_n is greater than one, a nonlinear enhancement effect is observed in the ion yield due to the usage of cluster projectiles. Cluster investigations showed an increase of SI yield over that of atomic beam sources, notably for higher mass species which were more likely to be fragments under bombardment with an atomic beam. One of the first cluster sources using SF_6 showed an enhancement factor of 10-25x compared to an atomic Cs^+ projectile, even though they have similar masses[9]. Around the same time, CsI clusters were produced as primary ions and showed an enhancement of the molecular ion of $\sim 50x$ [10].

In search of more massive clusters, C_{60} projectiles were studied as primary ions. In 1996 VanStipdonk et al. reported C_{60}^+ impacts on phenylalanine produced molecular ion yields 17x greater than the atomic projectiles Cs^+ and Ga^+ using the same impact energy[11]. Further studies by Vickerman et al. in 2003 showed the promise of an

effusion C_{60} source that could produce multiply charged ions via electron impact ionization[12, 13]. Moving from a singly to double charged projectile allows for a doubling of the impact energy which again increased SI yields $\sim 2x$.

Liquid metal ion sources (LMIS) allowed Benguerba et al. to study the enhancement factors using gold clusters (Au_n^q q=1-2, n=1-5) and the molecular ion yields of phenylalanine increased with increasing cluster size [14]. Later experiments with larger projectiles show a return to linear ion yield enhancement once more than 9 gold atoms were included in the bombarding cluster.

Massive cluster bombardment, utilizing Au_{400} clusters, found a 1000x enhancement in molecular ion yield over an atomic gold projectile with identical energy per charge for a target of gramicidin s[15]. This source has been utilized in the Schweikert group on a floated high voltage platform allowing for impact energies of 110-130 qkeV. This source shows that in this hypervelocity regime the Au_{400} cluster enjoys yield enhancement of deprotonated molecular ions and in ion multiplicity, meaning that a greater number of ions are created from each individual impact (Figure 1.2).
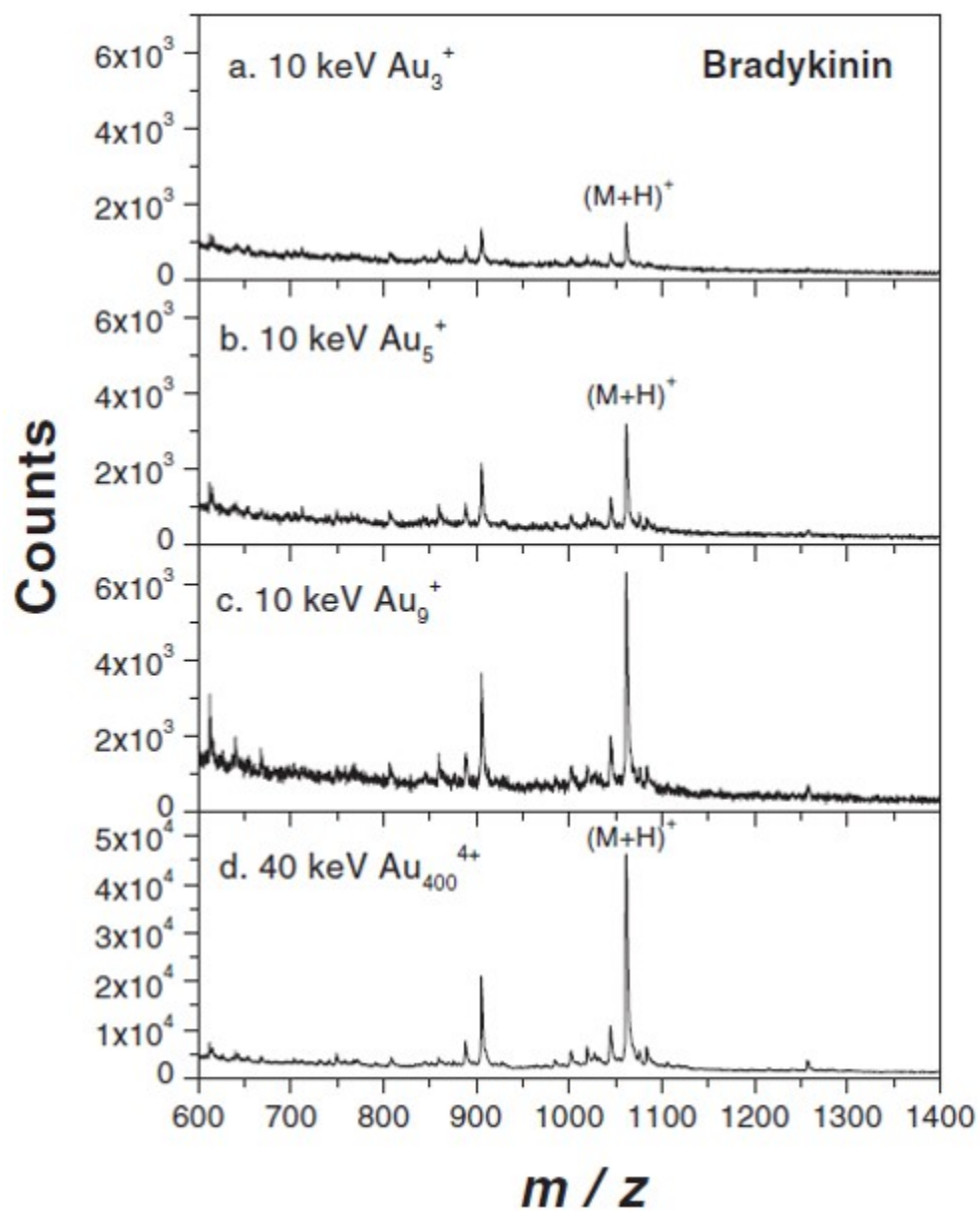
Figure 1.2: Ion Yield as a Function of Projectile Size

2. INSTRUMENT AND METHODOLOGY

This chapter details the instruments and methodology that were used in the following studies. The instruments are comprised of two custom built time-of-flight secondary ion mass spectrometers, one with a C_{60} effusion source and another with a floated gold liquid metal ion source. The methodologies permitted by the event-by-event bombardment and detection scheme allowed by these instruments provide for the extraction of mass spectra specific to nano objects and their surrounding chemical environments.

2.1 Au_{400} Instrument

Chapters III, IV, and VI present results obtained using a floated Au LMIS SIMS. A schematic is provided in Figure 2.1 [16]. This source is installed on the Pegase high voltage platform, designed and built by collaborators at the Institute of Nuclear Physics in Orsay (IPNO) France [17]. This platform can be biased to 100 kV, allowing for final projectile energies of up to 130 qkeV. The vacuum chamber containing the LMIS on the platform is maintained at $< 1x10^{-6}$ torr by a 400 L/s turbo pump (Adixen ATP400, Alcatel Vacuum Technology) backed by a mechanical rotary pump (Adixen 2015 SD).

The LMIS is comprised of a tungsten wire coil that forms a reservoir that is filled with Au/Si eutectic (97% Au, 3% Si, Academy Precision Metals). A procedure for the production of the source is given in Appendix A. When installed, the eutectic is melted through the use of an electric current of ~ 2 amps. This reservoir has a tungsten needle inset within, which when a high voltage (5-10 kV) is applied sees the formation of a Taylor cone at the tip, where a continuum of gold projectile sizes is created. The source is floated an additional 20 kV above the platform voltage,
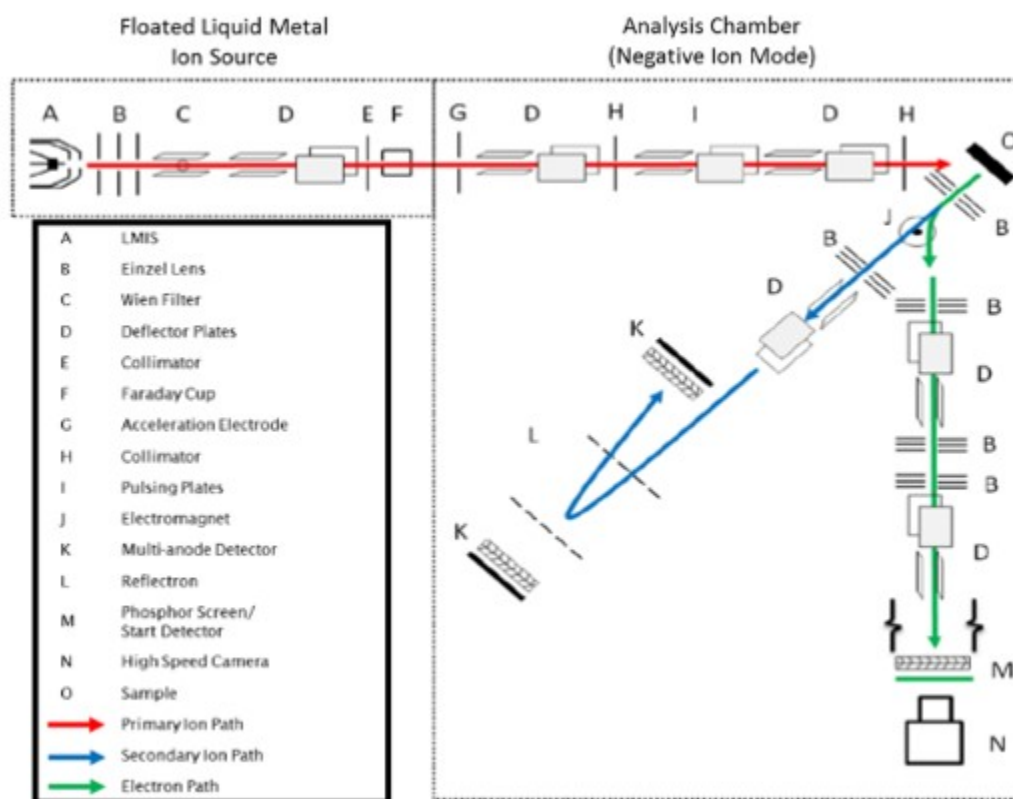
Figure 2.1: Schematic of Gold LMIS Instrument

providing a total kinetic energy of 120 qkeV upon exit of the platform.

While the source creates a continuum of gold projectiles, Au^+ to Au_{120q}^{q+} (q=1-9) the emission of massive clusters can be increased by increasing the extraction current applied. At 20 μm the distribution of clusters is centered around m/q 8,000 but at 50 μm the center is shifted to m/q 20,000 which corresponds to Au_{400}^{4+} [18]. The gold ion beam is focused using an Einzel lens into a Wien filter that is used to mass select projectiles with a desired mass to charge ratio (Figure 2.2).
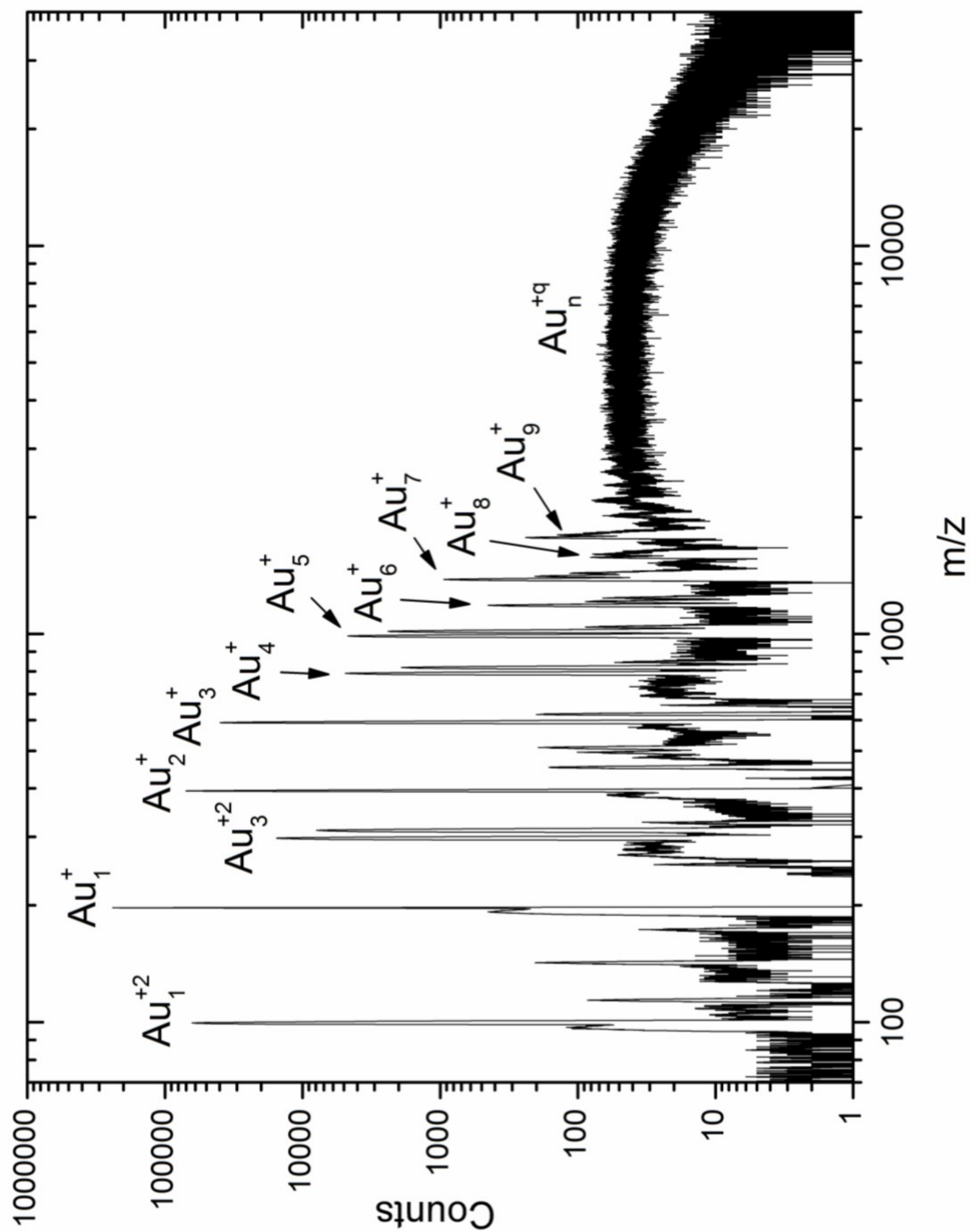
Figure 2.2: Gold Clusters Produced from LMIS Source

After selection of projectiles of interest, the beam is steered using horizontal and vertical electrostatic deflectors before passing through a collimator with one of four diameters (3 mm, 1 mm, 500 μm, or 200 μm). This collimation reduces the beam diameter and brightness while also defining the beam trajectory. All studies presented here utilized the 500 μm aperture. The beam intensity is measured using a removable Faraday cup after the collimator. Typical Au_{400} beam intensities are 150-300 pA utilizing a 20 μA extraction current.

An insulated coupler between the floated platform and analysis chamber is required to maintain the potential drop. This region is pumped using a 80 L/s turbo pump (Adixen ATP 80) to maintain a pressure of $\sim 1x10^{-6}$ torr. Three sets of deflectors are then used to direct the Au beam to the target surface in the analysis chamber. Between the first and second deflector, a collimator with two slits (0.5 and 1 mm) is positioned to block the passage of stray projectiles. The second deflector is also part of a pulsing system used to reduce the primary ion flux to that of $\sim$1000/s to achieve static SIMS conditions. A high voltage switch (Behlke HTS 151-03-GSM), driven by a pulse generator (HP 8005B) applies high voltage logic pulses to the vertical deflection plate. The pulsing voltage sweeps from +1 kV to -1 kV at a rate of 5 kHz. Before impact on the sample surface, the pulsed projectiles pass through another collimator containing four apertures (250 μm, 500 μm, 1 mm, 5 mm) to confine the bombardment region and to eliminate any stray trajectories passing from the pulsing region.

The sample target is biased at -10 kV, giving a final impact energy of 130 qkeV to the projectiles. These projectiles bombard at 45° , causing the emission of secondary ions and electrons which are accelerated from the target surface by a 10 kV Einzel lens. The focal point of this lens is within a weak magnetic prism ($\sim$ 30 Gauss) which is sufficient to deflect electrons but does not strongly influence the trajectories

of the heavier secondary ions. A series of lenses and deflectors direct the electrons which are detected by an electron emission microscope (EEM). The EEM consists of two microchannel plates (MCPs, Photonis) in a chevron configuration followed by an aluminized P43 phosphor screen. The phosphor allows for the visual detection of the electron cascade resultant from electron impact on the MCPs, allowing for the optimization of electron detection. These electrons start the ToF measurement for a single impact.

Secondary ions travel into a dual stage reflectron mass spectrometer after passing through another Einzel lens [19]. These ions are reflected by an ion mirror at 2.8° from their incident trajectories and are subsequently detected by another chevron MCP pair. The anode of this detector consists of a pie shaped eight anode detector, which allows for the detection of up to 8 isobaric ions from each individual impact. A pair of deflectors in the entrance to the reflectron allow for the optimization of SI trajectories by distributing ions evenly across all eight anodes.

A charged particle impacting the chevron MCP assembly will be amplified to a flux of $\sim 10^6$ electrons which can then be detected as a negative voltage pulse on an anode. This pulse is sent to an eight port constant fraction discriminator (CFD Ortec CF8000). The CFD eliminates ringing on the anode by setting a pulse amplitude threshold and then converts any pulse above this threshold to a Nuclear Instrumentation Module (NIM) logic pulse to stop the ToF measurement. Pulses from the electron start detector are converted using a similar quad CFD (Canberra QUAD454). The logic pulse signals for the start and stop are transferred to a time-to-digital converter (TDC, Orsay Physics ISIBOX). After receiving a start signal, stop signals are time registered relative to the start with a time resolution of 120 ps. The signal from each individual projectile impact, consisting of a start and all related stops, are recorded as a single event. The accumulation of several million

events over the course of an experiment are stored as an EDF file type. EDF files are then processed by custom analysis software, SAMPI (Surface Analysis and Mapping of Projectile Impacts) [20].

2.2 C_{60} Instrument

The study presented in chapter V contains data obtained from the operation of a custom built effusion source C_{60} SIMS instrument with a linear ToF mass analyzer. A diagram is presented in Figure 2.3.

C_{60} ions are generated by heating buckminsterfullerene powder (Sigma Aldrich) in a copper oven to its sublimation point ($\sim 450°$ C). Gaseous C_{60} effuses out through an aperture into an ionization region where it is ionized by electron impact to C_{60} q^+ (q=1-3) using a tantalum electrode that emits 150 eV electrons. Ionized C_{60} are accelerated at either 10 or 15 qkeV toward an extraction plate and focused by an Einzel lens. Deflectors then steer the ion beam into a Wein filter to facilitate the selection of a single charge state. The selected beam is then directed toward a -10 kV target at 45°. Unlike the Au system, a pulsing system is not required as the ion flux is tuned by the electron emission from the Ta electrode, satisfying the requirements for event-by-event bombardment detection. Detection and processing of secondary ions and electrons is similar to that of the Au instrument.

2.3   Wien Filter

Wein filters are velocity filters that consist of a static magnetic field perpendicular to a variable electric field between two electrodes. The net effect between Coulombic and Lorentzian forces define the trajectory of a charged particle or ion within the Wien filter.

$$F_{net} = (qE) + (qv * B) \tag{2.1}$$
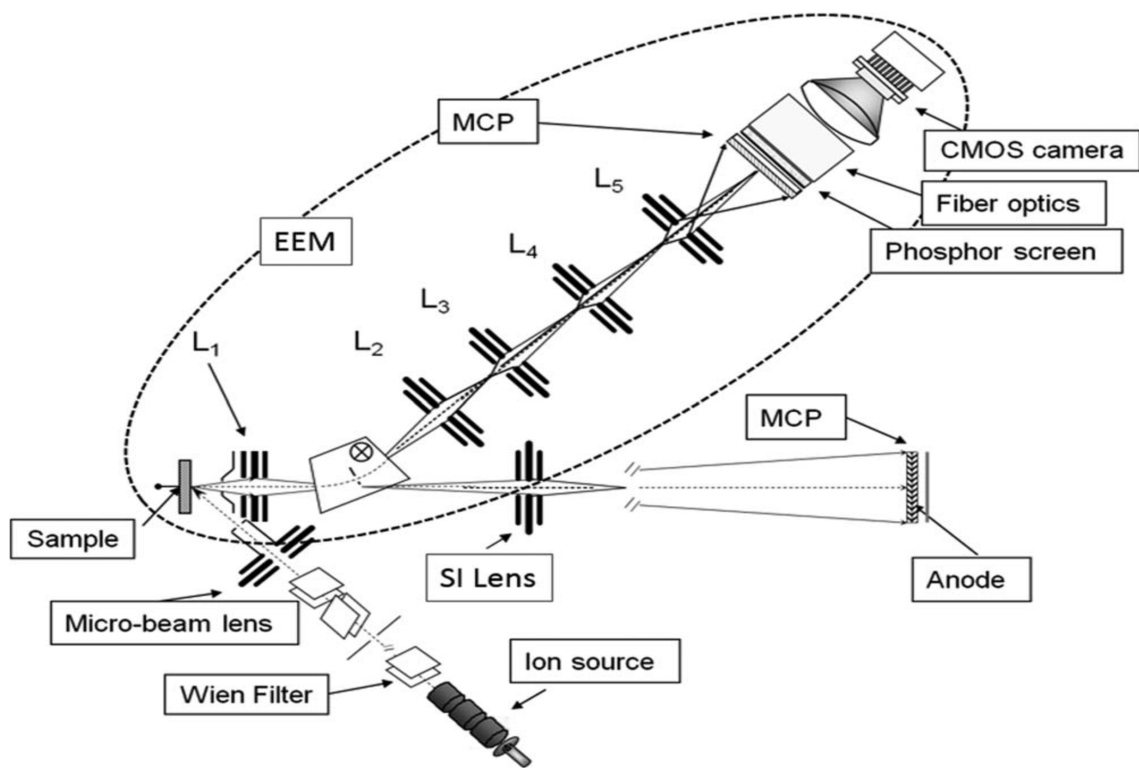
Figure 2.3: Schematic of C_{60} Instrument

Where E and B are the electric and magnetic field strengths in Tesla and v is the velocity (m/s) of the particle. By varying the electric field, it is possible to produce a net zero force for a given velocity, allowing for a linear trajectory to pass through the filter.

$$qE = qvB \tag{2.2}$$

$$v = \frac{E}{B} = \frac{\frac{V}{d}}{B} = \frac{V}{dB} \tag{2.3}$$

Where V is the voltage applied and d is the distance (meters) between electrodes.

The velocity of an ion is determined by its kinetic energy (E_k, joules) and its mass (m, kg)

$$v = \sqrt{\frac{2E_K}{m}} \tag{2.4}$$

Combining equations 2.3 and 2.4 gives the voltage required to select a projectile of a desired mass

$$V = Bd\sqrt{\frac{2E_K}{m}} \tag{2.5}$$

2.4   Time of Flight Mass Analyzer

The secondary ion flight time is characteristic of its mass to charge ratio (m/z), and for a linear ToF, the total flight time is given by the summation of the times spend in the acceleration, drift, and deceleration regions of the mass spectrometer. The acceleration region is from the sample surface to the extraction lens, the drift region is the field free zone between two grounded lenses or grids, and the deceleration region is from the grounded grid to the negative potential applied to the front of the MCP assembly.

$$t_{total} = t_{ac} + t_{dr} + t_{de} \tag{2.6}$$

The derivation of equations calculating the time spent in each region is detailed elsewhere and are shown below

$$t_{ac} = \sqrt{\frac{2md_{ac}^2}{qV_{ac}}}$$

(2.7)

$$t_{dr} = \sqrt{\frac{md_{dr}^2}{2qV_{dr}}}$$

(2.8)

$$t_{de} = \frac{\sqrt{2md_{de}^2} * (-\sqrt{V_{ac}} \pm \sqrt{V_{ac} + V_{de}})}{\sqrt{q} * V_{de}}$$

(2.9)

Therefore,

$$t_{total} = \sqrt{\frac{2md_{ac}^2}{qV_{ac}}} + \sqrt{\frac{md_{dr}^2}{2qV_{dr}}} + \frac{\sqrt{2md_{de}^2} * (-\sqrt{V_{ac}} \pm \sqrt{V_{ac} + V_{de}})}{\sqrt{q} * V_{de}}$$

(2.10)

Where t_{ac}, t_{dr}, and t_{de} are time spent in acceleration, drift, and deceleration regions, respectively, m and q are the mass and charge of the ion, V_a is the target voltage, V_d is the detector voltage applied to the front of the MCP assembly, d_{ac}, d_{dr}, and d_{de} are the lengths of the acceleration, field free, and deceleration regions, respectively.

For a reflectron ToF, it is required to calculate the time spent in the ion mirror region as well. The ion mirror is made from successive grids with progressively increasing negative voltages applied with the final grid having a voltage higher than that of the acceleration potential applied in the acceleration region. A penetrating ion is retarded by the increasingly strong electric fields until it is reflected. The depth of penetration determines the time spent in this region and is given by

$$qV_{ac} = q\frac{V_{ref}}{L} * d_{ref}$$

(2.11)

16

And rearrangement gives

$$d_{ref} = \frac{V_{ac}L}{V_{ref}} \tag{2.12}$$

Where L is the length of the reflectron. The time to reach this depth is given by

$$t_{\frac{ref}{2}} = \frac{d_{ref}}{\frac{v}{2}} \tag{2.13}$$

Where v is the velocity of the ion when exiting the acceleration region. The time spent in the reflectron is given by

$$t_{ref} = 2 * t_{\frac{ref}{2}} = \frac{4d_{ref}}{v} = \frac{4d_{ref}}{\sqrt{\frac{2qV_{ac}}{m}}} = \sqrt{\frac{8md_{ref}^2}{qV_{ac}}} \tag{2.14}$$

Therefore, in a reflectron ToF mass spectrometer the total time from production to detection is given by

$$t_{total} = t_{ac} + t_{dr1} + t_{ref} + t_{dr2} + t_{de}$$
$$= \sqrt{\frac{2md_{ac}^2}{qV_{ac}}} + \sqrt{\frac{md_{dr}^2}{2qV_{dr}}} + \sqrt{\frac{8md_{ref}^2}{qV_{ac}}} + \sqrt{\frac{md_{dr}^2}{2qV_{dr}}} + \frac{\sqrt{2md_{de}^2} * (-\sqrt{V_{ac}} \pm \sqrt{V_{ac} + V_{de}})}{\sqrt{q} * V_{de}}$$
$$\tag{2.15}$$

For both linear and reflectron ToF mass analyzers it is shown that the flight time is proportional to the square root of an ions mass (Eq 2.10, Eq 2.15). As such it is possible to convert from a time to a mass spectrum by using a mass calibration where two or more data points are fitted to Equation 2.16, where a and b are the slope and the intercept of a fit trendline, respectively.

$$t_{total} = a\sqrt{m} + b \tag{2.16}$$

2.5   Event-by-Event Bombardment

The use of the pulsing system detailed previously ensures that individual projectiles are separated in both time and space, approximately 1 ms apart. As each projectile is recorded individually, this methodology is termed event-by-event bombardment detection and is classified as a super static regime where the projectile dose is less than 10^6 projectiles per cm^2 [21]. This allows for the reasonable assumption that each impact is on fresh sample and perturbing the same spot twice has a low probability. The secondary ions from each impact are recorded as a single, independent event. A conventional mass spectrum can be obtained by summing all the events from a measurement. An ion of interest will have a secondary ion yield, Equation 2.17, that describes the production efficiency from a single impact.

$$Y_A = \sum_{x_A} \frac{x_A N(x_A)}{N_{total}} = \sum_{x_A} x_A P(x_A) = \frac{I_A}{N_{total}} \tag{2.17}$$

Where x_A is the number of detected ions A in a single event, $N(x_A)$ is the number of events that contain ion A with x_A detected, N_{total} is the total number of events in the measurement, $P(x_A)$ is a probability distribution describing the number of ions A that are emitted from a single impact, and I_A is the number of detected ions A from the total mass spectrum.

Cluster projectiles are efficient at producing multiple ions per impact and with the use of event-by-event methodology it is possible to determine the number of ions emitted from a single impact, known as the multiplicity. Using SAMPI it is possible to calculate the total number of ions emitted from a single impact, known as total ion multiplicity, and the number of a specific ion of interest emitted per impact, or ion selected multiplicity.

2.6   Ion Coincidence

Since each impact is recorded as an individual event, it is possible to interrogate the data by selecting out a subset of impacts where an ion of interest is emitted. A coincidental mass spectra is produced by summing all events where this subset is observed Figure 2.4. The coincidental mass spectrum is populated only with secondary ions emitted from the same nanovolume as the ion of interest, so they must be co-located within 5-10 nm [22, 23].
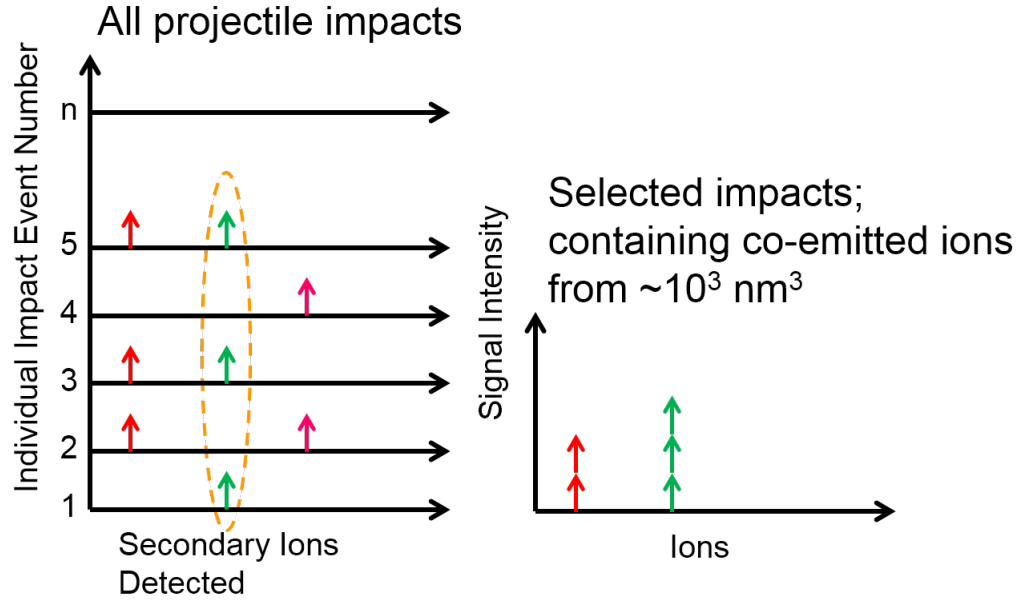
Figure 2.4: Event-by-Event Collection and Coincidental Analysis

2.7   Effective Yields and Coverage

The surface coverage of an analyte on a targets surface can be calculated using the coincidental methodology. After determining effective impacts (N_e), i.e. the number of impacts on the analyte, the ratio of effective impacts to the total number

of impacts will provide the analyte coverage within the analysis area. Two ions, A and B, that are characteristic of the analyte are required to calculate the number of effective impacts. If the two ions are assumed to be emitted independently of one another then the coincidental ion yield $Y_{A,B}$ is the product of the secondary ion yields of A and B, shown in Equation 2.18

$$Y_{A,B} = Y_A * Y_B \tag{2.18}$$

Therefore, Equation 18 can be rewritten similarly to Equation 17

$$\frac{I_{A,B}}{N_{eff}} = \frac{I_A}{N_{eff}} * \frac{I_B}{N_{eff}} \tag{2.19}$$

Where I_{AB} is the number of events where A and B are both detected, I_A is the number of events containing ion A and I_B is the number of events containing ion B. N_{eff} is the number of effective impacts with coemission of ions A and B. By rearranging Equation 2.19, the coverage K can be determined.

$$K = \frac{N_{eff}}{N_{total}} = \frac{I_A * I_B}{I_{A,B} * N_{total}} \tag{2.20}$$

3. CHARACTERIZATION OF SURFACE COATING COVERAGE ON GOLD NANORODS*

3.1 Introduction

Synthesis of Au nanorods (NR) is made possible by surfactant molecules such as cetyltrimethylammonium bromide (CTAB) which show preferential adsorption onto specific crystal facets[24]. This adsorption prevents further reduction of Au^+ on these faces, directing the growth of asymmetrical nanoparticles[25]. The adsorption of a CTAB bilayer 3-4 nm in thickness has been shown previously to resist removal through chemical or physical techniques [26, 27], but the replacement of this layer after NR production is important due to the high cytotoxicity exhibited by CTAB coated NRs. These NRs have potential for use in drug delivery, bioimaging, and DNA or peptide based assemblies if enough CTAB can be replaced with another functional coating to prevent toxicity and direct function [27].

Methods to remove CTAB have been reported in the literature with functionalization with peptides[28], antibodies[29], or polyethylene glycol[30]. These strategies require multiple reaction steps and often result in the loss of colloidal stability of the NR. Oxygen plasma treatment has also been studied as a removal technique but tends to promote fusion of the metal cores[27].

Presently, there are few techniques for the characterization of Au NR surface coatings due to the difficulty of producing monodisperse rods at high enough concentrations for most widely used scattering methods. Small angle neutron scattering has shown to be a useful analytical technique for characterization of surface coatings of these samples, however they disagree with mass spectrometry measurements as to

---

whether removal of the CTAB moiety is possible[31].

Here, we present a study to determine the surface coating of CTAB on Au NRs using secondary ion mass spectrometry where effects of the core NR size are greatly reduced in comparison to bulk averaging techniques. Run in the event-by-event bombardment/detection regime, SIMS can be used to probe nanometer volumes and characterize individual Au NRs. For high concentration samples such as the ones studied here, impacts also occur on interface zones between two NRs but as the rods are larger than the probed volume ensemble averaging is avoided. The coating of CTAB is first determined for as-produced Au NRs and then samples are washed with either ethanol or chloroform to see if the soluble CTAB molecules can be washed from the core NR.

3.2   Method

A custom gold cluster SIMS instrument was used for these experiments, running in the event-by-event bombardment/detection mode. Briefly, gold clusters (Au_{400}^{4+}) are produced and accelerated to 520 keV to bombard a sample. The beam of Au_{400}^{4+} is pulsed to a repetition rate of 3 kHz so that each impact is separated in time and space. After impact with the sample, secondary ions and electrons are produced and extracted into two analysis regions. A magnetic field deviates electrons to a microchannel plate detector that starts the time of flight measurement while secondary ions travel through a reflectron time of flight mass analyzer to an 8 anode microchannel plate detector that stops the time measurement.

Each individual impact and emitted secondary ions are stored individually on a computer system that allows for the interrogation of the data as individual sets. A conventional mass spectrum is produced by summing all impacts together but it is also possible to sum only events containing as secondary ion of interest, such as one

coming from the CTAB moiety. This is termed a coincidental mass spectrum and allows for the display of all secondary ions that are co-emitted with the selected ion of interest. Since these ions must be collocated on the surface within the emission volume, information about the chemical environment is obtained.

Samples were obtained from the Zubarev lab located at Rice University in Houston, TX. These as-prepared samples were aqueous suspensions of Au NRs coated by CTAB. The samples were prepared for analysis by drop casting onto silicon wafer squares and allowing the water to evaporate. An ethanol atmosphere was utilized in order to overcome the ringing effect commonly produced when dropcasting nanoobjects from water. Ethanol vapor reduces the surface tension and drives a circulating current within the water drop, continuously mixing the nanorods and prevent aggregation. These samples are then introduced into a vacuum chamber for analysis using the Au_{400}^{4+} projectile. Approximately $3x10^6$ impacts were performed for further analysis.

3.3   Results and Discussion

Figure 3.1 shows the mass spectrum obtained with characteristic peaks labeled. CTAB peaks were determined by running a pure CTAB sample to find corresponding peaks.
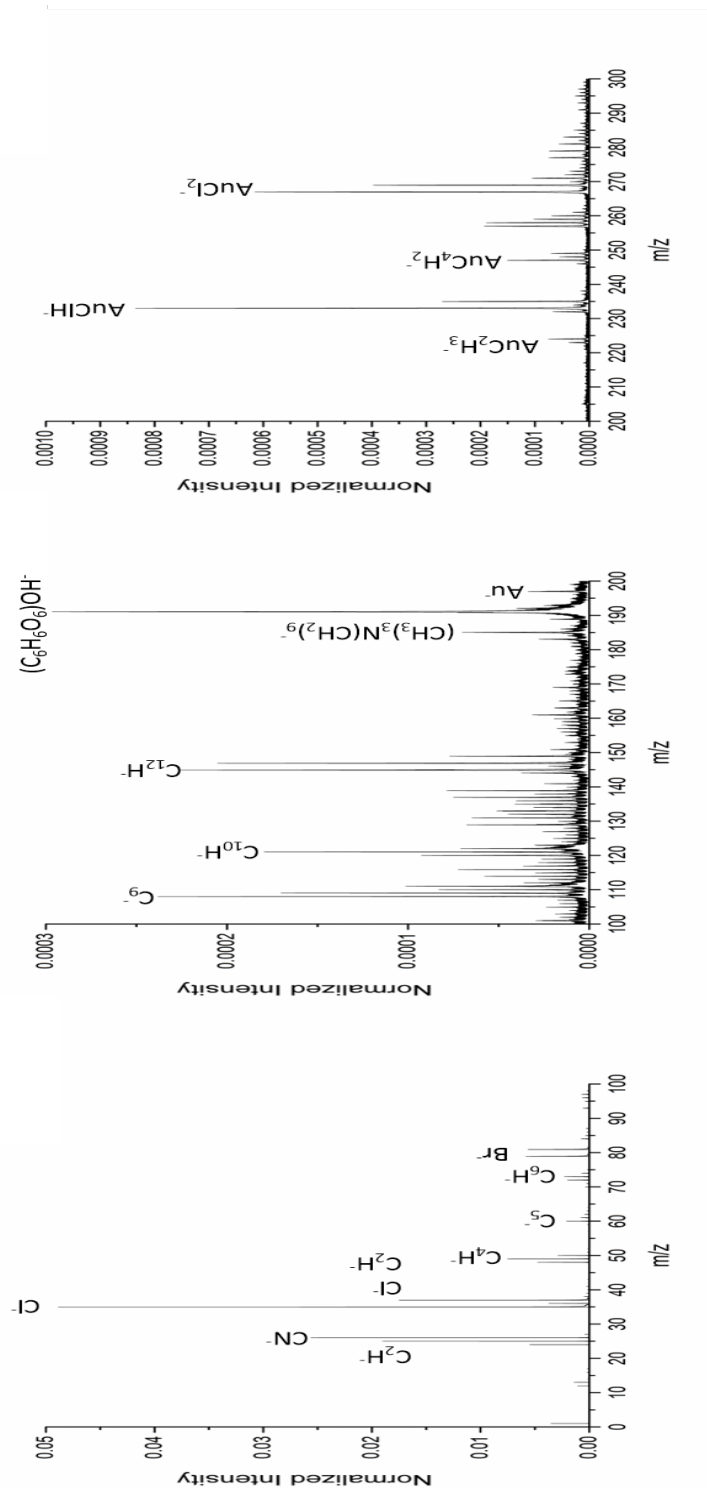
Figure 3.1: Mass Spectra of Dropcast Au NRs

Peaks arising from the gold NR are present throughout the spectra but larger gold clusters are conspicuously absent. For other gold nano objects, emission of Au_x clusters are commonly seen and with such relatively large dimensions it would be expected to observe these clusters for a gold nanorod. The absence of these peaks leads to the conclusion that the CTAB coverage is high enough to prevent ion emission from the metal core. CTAB bilayers are expected to be between 3-4 nm, much less than previously observed emission depths, however the low atomic z overlap and low density nature of the CTAB- Au_{400}^{4+} interaction must prevent sufficient energy deposition into the gold core. It may also be possible that the CTAB screens the secondary ions produced and prevents their extraction for analysis.

CTAB peaks are observed in the mass spectrum as well, with $BrC_5H_6^-$ observed as a prominent fragment of the CTAB hydrocarbon chain. Brominated peaks are present throughout the spectrum as the CTAB counterion combines with fragments from the hydrocarbon chain.

A large ion peak is observed at m/z 191 which corresponds to $(C_6H_6O_6)OH^-$ which arises from dehydroascorbic acid in the sample. This oxidized form of ascorbic acid is to be expected as ascorbic acid is used in the synthesis of Au NRs to reduce gold ions into Au(I) seeds. Further reduction occurs with the Au(I) acting as a catalyst, ensuring reduction only occurs on seed surfaces.

To test the removal of the CTAB coating after the Au NRs were drop cast onto silicon they were then immersed in either ethanol or chloroform, in which CTAB is known to be soluble. After 5 minutes of immersion the samples were allowed to evaporatively dry and were then introduced into vacuum. Again $\sim 3x10^6$ impacts were recorded. Figure 3.2 shows the total mass spectra of the unwashed and two washed samples for comparison.

Washing with ethanol proved to have little effect upon the sample, however wash-

ing with chloroform removed a significant portion of the deposited Au NRs. While CTAB is soluble in both rinsing solutions, the chloride may be expected to compete with the Br counterion in CTAB, disrupting the physisorption with the silicon support and allowing a portion to be washed away. This reduction in sample coverage is observed in the comparison spectra as a reduction in peak intensities, note the difference in scale for chloroform rinsing spectra in Figure 3.2. Washing produces CTAB fragments not observed in the untreated sample, notably at m/z 169, 171, and 173, arising from $Br_2CH_x^-$ where x= 0, 2, or 4.

Figure 3.2: Effects of Washing on Total Mass Spectra of CTAB Coated Au NRs
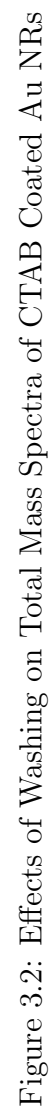
Table 3.1: Surface Coverage of CTAB Based on Solvent Treatments

Ion Pair	No Wash	EtOH Wash	CHCl$_3$ Wash
Au/AuClH	52%	55%	22%
Au/AuCl$_2$	45%	55%	∼0%
^{79}Br/^{81}Br	99%	91%	43%
^{79}Br/Br$_2$(CH$_2$)$_{10}$(CH$_3$)	89%	87%	∼0%

Surprisingly, longer chains of CTAB ions show reduction after washing. The BrC$_5$H$_6^-$ ion is prominent in the unwashed sample but nearly absent in washed samples. Likely this is due to unbound CTAB being washed away as excess CTAB is present in solution during synthesis but but bound CTAB remains on the nanorod.

Using a pair of characteristic peaks, it is possible to calculate the surface coverage of specific moieties. Using Equation 2.20, coverage is calculated from ion pairs that arise from either the CTAB coating (^{79}Br/^{81}Br and ^{79}Br/Br$_2$(CH$_2$)$_{10}$CH$_3$) or from the gold nanorod (Au/AuClH and Au/AuCl$_2$)

Table 3.1 shows the calculated coverages for both gold ions from the nanorod and CTAB coating. It is shown that washing with ethanol has little to no effect on the coverage of Au NRs or CTAB. Chloroform washing shows a drastic decrease in both coverages, but taking a ratio of CHCl$_3$ to unwashed sample gives a similar (∼40%) reduction in coverage. This is due not to CTAB being removed from the Au NR but from the physical removal of the entire NR structure from the silicon wafer as was discussed before.

3.4   Conclusions

The removal of a CTAB layer on gold nanorods using chemical solvation has been shown to be ineffective. While soluble in methanol and chloroform, CTAB rinsed with these solvents does not detach from the nanorod. Using a nonpolar solvent such as chloroform over a polar aprotic solvent like methanol will remove the nanorods

from the surface while leaving the CTAB layer unchanged.

These results agree with previous studies which show the removal of a CTAB layer through chemical means is very difficult as only invasive techniques such as oxygen plasma treatment are likely to be able to remove the bilayer formed.

Importantly, a new instrumental method is described for the surface coverage analysis of nanoparticles. Crucially, the event-by-event bombardment SIMS technique samples individual nano-objects and therefore prevents ensemble averaging. This allows for broader size distributions to be analyzed which is not possible in spectroscopy techniques as the wavelength is dependent on the dimensions of the core nanorod.

This technique also reduces the need for large amounts of sample needed for powder scattering techniques, as a single deposited layer is sufficient for the analysis of surface coverage. Future modification techniques can be tested for efficacy using this unique approach.

4. CHARACTERIZATION OF NANOMETRIC INCLUSIONS VIA NANOPROJECTILE IMPACTS*

4.1 Introduction

It has been shown that sputter and secondary ion yield from nanoparticles, NPs, in sizes below a few tens of nanometers are size dependent[32]. We refer here to dimensions which are not sufficient for complete projectile energy deposition in a direct collision between the incident ion and the nano-object. Grazing and interfacial collisions further complicate the nature and abundance of the ejecta. The non equivalency of impacts can clearly affect the accuracy of NP analysis. However, when NPs are ultra-small (<10 nm) they can be completely fragmented/atomized in one collision, thus all impacts should be equivalent. We examine here this case and its consequences for characterizing ultra-small NPs and their chemical environment. The samples were aggregations of gold atoms, specifically 55, 147, or 225 atoms encapsulated within a poly(amido amine) dendrimer. Encapsulation within a dendrimer structure prevents agglomeration of NPs, prevents passivation of catalytic surfaces, and can be used to control catalytic rates[33, 34, 35]. While most analysis techniques for the characterization of nanoparticles produce an averaged measurement due to the blending of sub ensembles within a population, it is possible to obtain accurate analysis of discrete ensembles by measuring each nano object individually. This approach allows for a nuanced method that returns both averaged data and separates sub ensembles based on the treatment of the data after analysis. The emission of characteristic gold adducts from the nanoparticle is detailed below.

The experiments were run in the event by event bombardment-detection regime, where a single projectile hits a NP coupled with the individual recording of the SIs from each impact. To be practical, this approach requires a projectile generating a large ion multiplicity[36]. The projectile of choice was Au_{400}^{4+}, itself a nanoprojectile of ~ 2 nm in diameter.

4.2 Preparation of Dispersed Dendrimer Encapsulated Nanoparticles

Au NPs were reduced from a solution of $HAuCl_4$ by excess $NaBH_4$ in the presence of generation 7 PAMAM dendrimers. The reduction to zero valent gold causes the aggregation and growth of gold into NPs, the size of which is controlled by the original concentration of $HAuCl_4$ in solution[37]. Au55, Au147, and Au225 were produced, corresponding to nanoparticle diameters of 1.3, 1.5, and 1.7 nm, respectively. Solutions of DENs were then drop cast onto Si (1 0 0) wafers after cleaning by sonication in absolute ethanol. Upon evaporation of excess solvent, a layer of DENs was produced where the gold NPs are isolated from one another due to the enveloping dendrimer structure.

4.3 Results and Discussion

Dendrimer encapsulation allows for the individual bombardment of a single nanoparticle at a time. Chemical information about the surrounding area can be obtained through co-emitted ions, but first characteristic ions must be classified. Table 4.1 shows ions that are representative of different chemical moieties within the sample. Ions arise from an impact on the Au NP or the surrounding dendrimer scaffolding. The dendrimer has two distinct chemical configurations, both of which are formed from the fragmentation of a dendrimer chain upon bombardment. The difference arises from whether or not the chain has undergone reductive damage from the $NaBH_4$ used during the synthesis of the Au NP. In the total mass spectrum, Figure
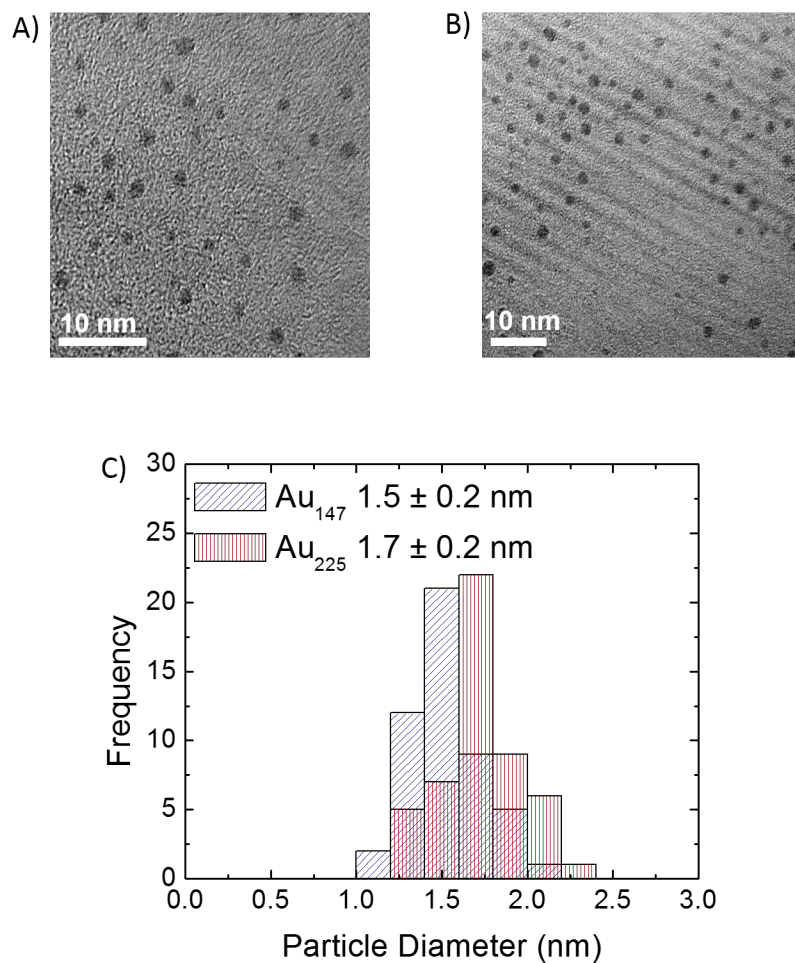
Figure 4.1: TEM Micrographs of Au147 (A) and Au225 (B) Nanoparticles. Size Distribution and Comparison in (C)

Table 4.1: Surface Coverages of Characteristic Gold and Dendrimer Moieties

Mass	Formula	Classification
420	Au_2CN^-	Gold
419	$Au_2C_2H^-$	Gold
394	Au_2^-	Gold
373	$C_{16}N_7O_3H_{35}^-$	Gold
249	$AuCN_2^-$	Gold
197	Au^-	Gold
109	$C_7H_{11}N^-$	Reduced
108	$C_7H_{10}N^-$	Reduced
93	$C_6H_7N^-$	Reduced
43	$C_2H_5N^-$	Reduced
42	$C_2H_4N^-$	Reduced
99	$C_5H_9O^-$	Native
84	$C_4H_6O^-$	Native
75	C_5NH^-	Native
50	C_3N^-	Native

4.2, there are peaks that arise from impacts on the native and reduced dendrimer structure, as well as on the Au NPs.
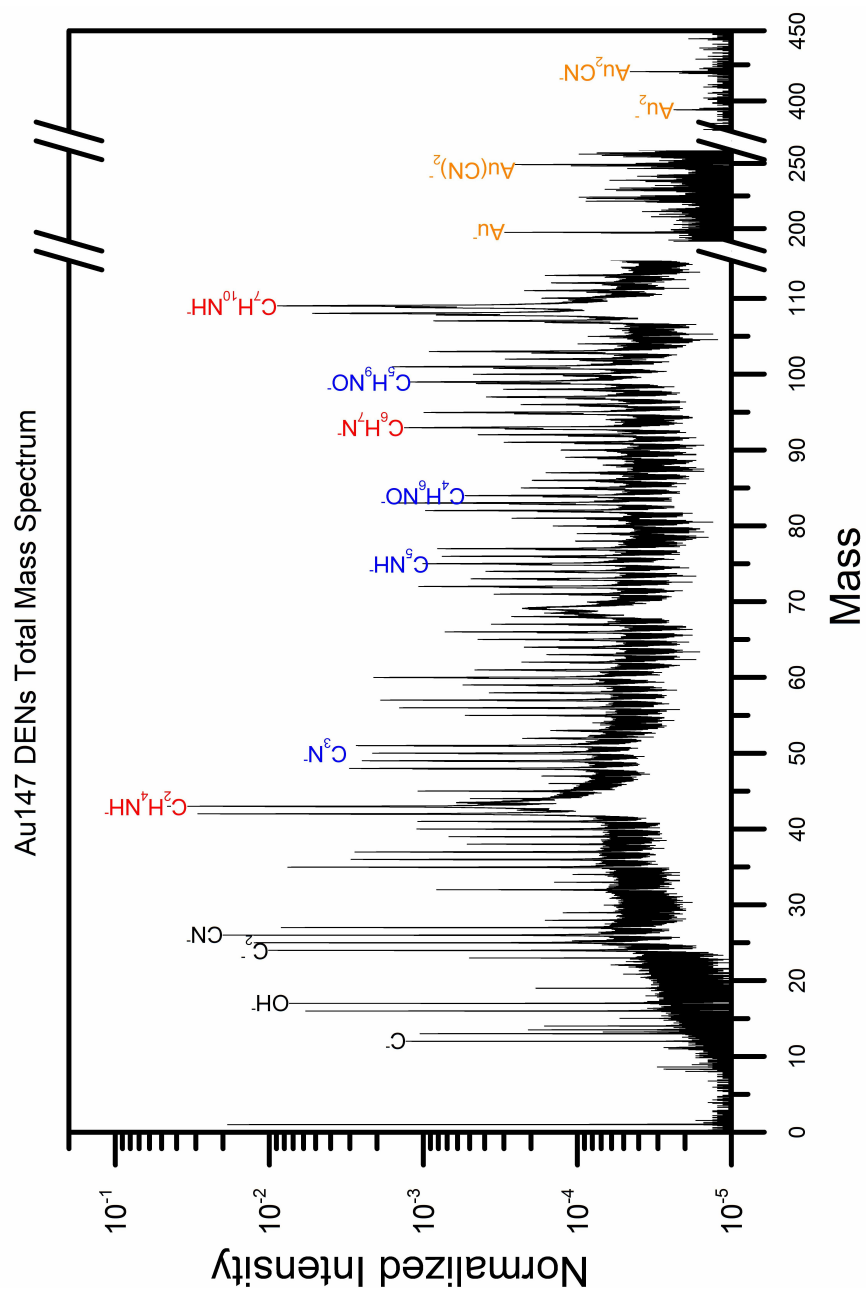
Figure 4.2: Total Mass Spectrum of Au147 Dendrimer Sample

With the coincidental methodology, it is possible to select SIs that arise from a specific impact. Since Au_2CN^- and $Au(CN)_2^-$ are only present in spectra with the bombardment of a Au DEN and not in a blank dendrimer sample , keying in on these two adducts allows for the selection of impacts of the Au_{400}^{4+} projectile with the Au NP without worrying about gold contribution from the projectile. With $Au(CN)_2^-$ set as the coincidental condition while evaluating the yield of Au_2CN^-, the emission of the gold adduct is enhanced as the size of the Au NP increases (Figure 4.4). This agrees with previous studies that have shown an increase in gold clusters from nanoparticles as the size of the NP increases.
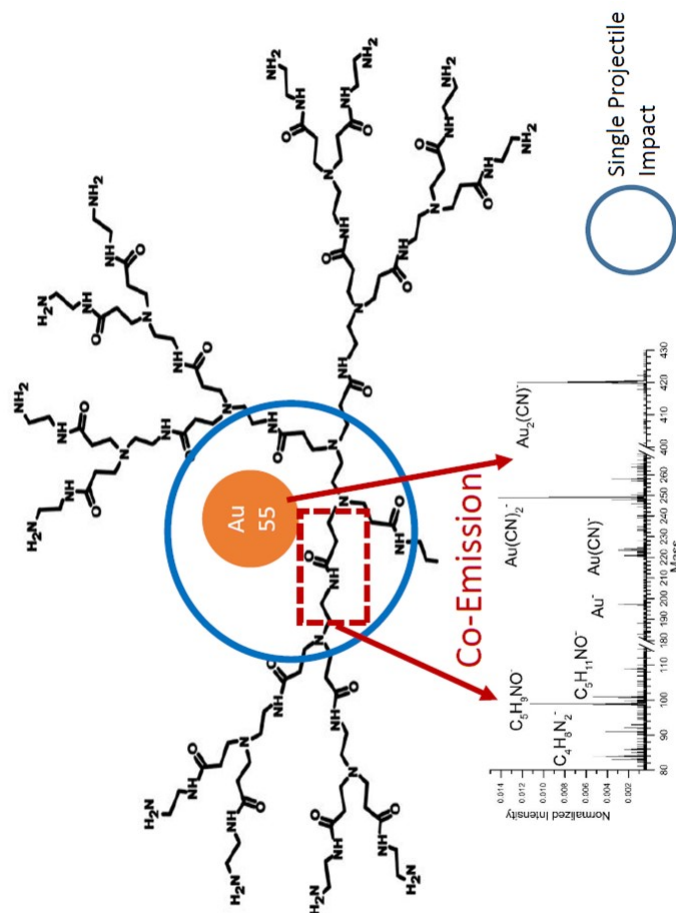
Figure 4.3: Bombardment and Coemission of Gold Nanoparticle and Surrounding Dendrimer Environment
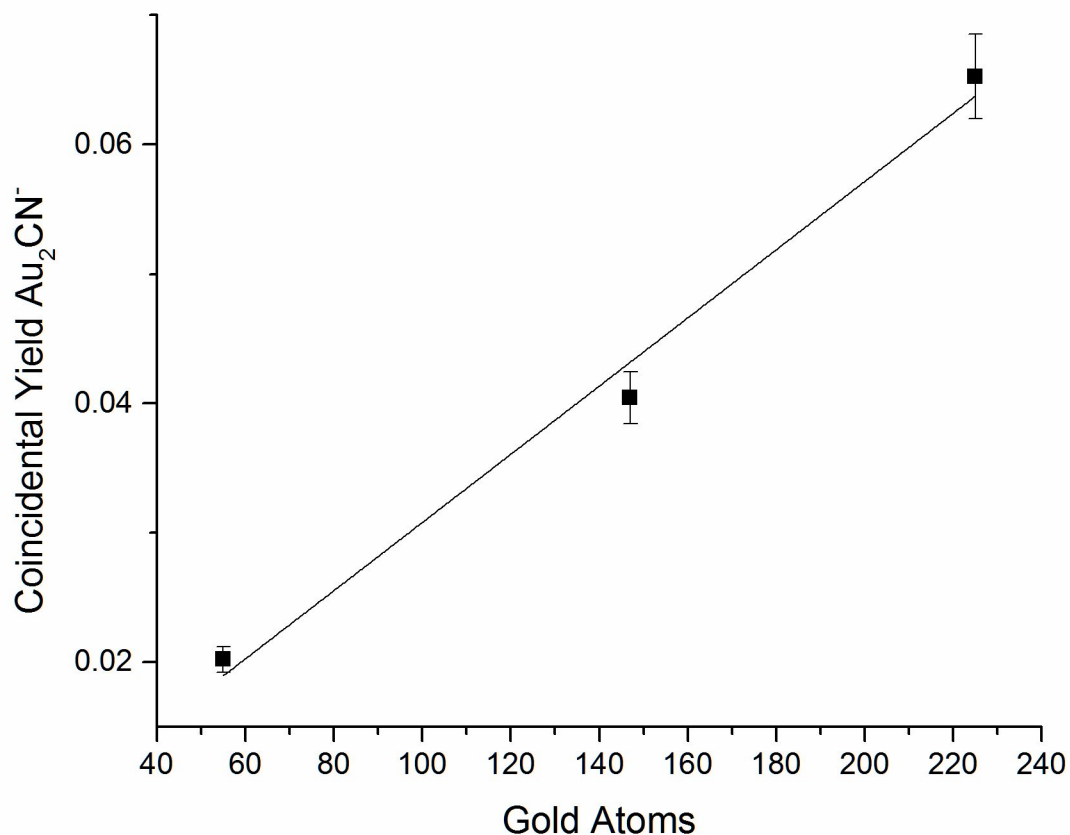
Figure 4.4: Coincidental Yield of Au_2CN^- as a Function of Constituent Gold Atoms

Utilizing characteristic ions identified as belonging to different portions of the sample, make it possible to use the coincidental methodology to probe the chemical environment around the NP. Using Equation 2.20 where $Y_{A,B}$ is the coincidental yield of ion A with ion B and Y_A is total yield of ion A, the co-emission of two ions can be evaluated. If ion (A) is coincidental with another ion (B) that signifies the two ions are co-emitted from an individual impact on the sample. The ratio of the coincidental yield to the total yield, where ratios above 1 show co-emission, and

37

therefore co-location, while ratios under 1 show chemical segregation of the two ions.

When ions belonging to the native dendrimer structure are emitted there is an increase of co-emission of characteristic gold ions. For example, when impacts containing $C_5H_9NO^-$ are selected, $Au(CN)_2^-$ the coincidental yield is 3 times larger than the total yield. Thus, there must be chemical co-location of less than 10 nm of the Au NP with dendrimer branches that have not undergone reductive damage. Conversely, it is shown that the co-emission of gold ions is lowered when reduced dendrimer fragment ions are co-emitted. The coincidental yield of $Au(CN)_2^-$ with $C_7H_{11}N^-$ is 1% of the total yield; therefore, the NP does not co-locate with damaged dendrimer regions during encapsulation (Figure 4.5). These results show that the Au NP preferentially grows in native dendrimer structure environments during synthesis which could be used to direct growth of NPs in future systems.

The Au NP size also affects the chemical environment of the dendrimer, shown in Figure 4.6. As the nanoparticle size increases from 55 to 225 atoms, there is a clear increase in the segregation of native and reduced dendrimer structures. This is evidenced by the decrease in the ratio of coincidental yield to total yield that signifies a reduction in the co-emission of two ions. Interestingly, characteristic gold ions have greater co-emission with native dendrimer structures and greater segregation from reduced dendrimer structures for larger NPs. This correlates well with the idea that Au NPs prefer native dendrimer structures as we expect greater reductive damage to the dendrimer during synthesis of larger NPs due to an increase in $NaBH_4$ used.
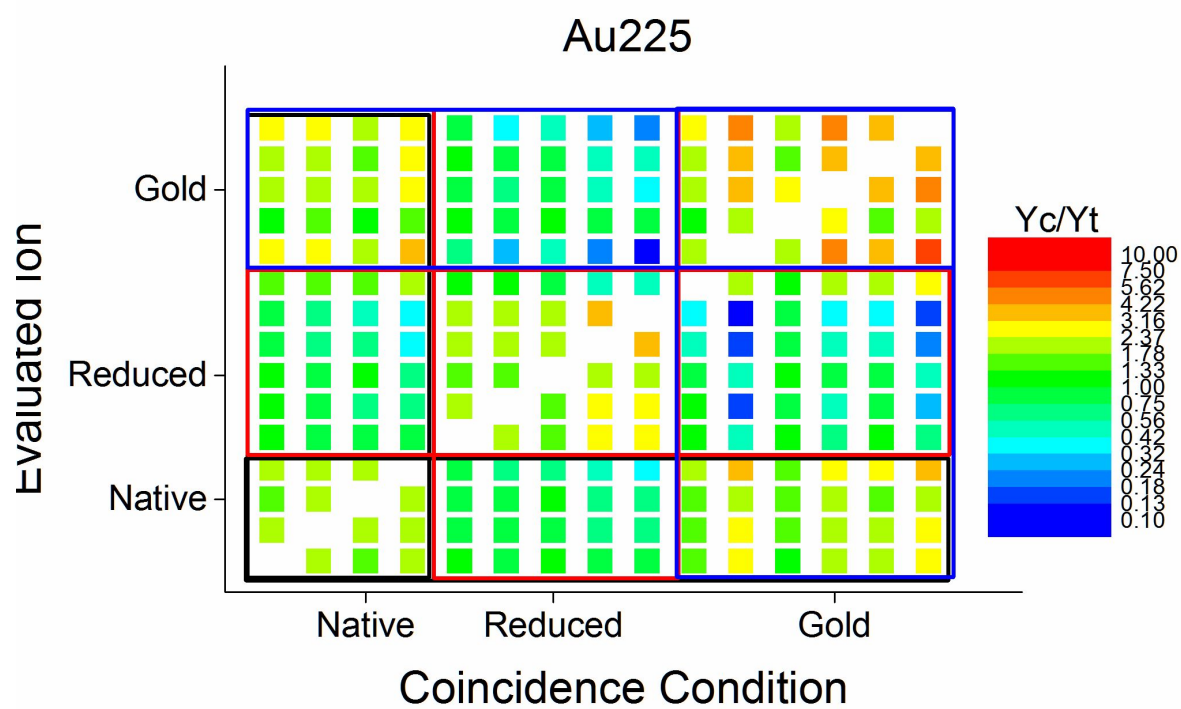
Figure 4.5: Yc/Yt Comparisons Based on Ion Type For Au225
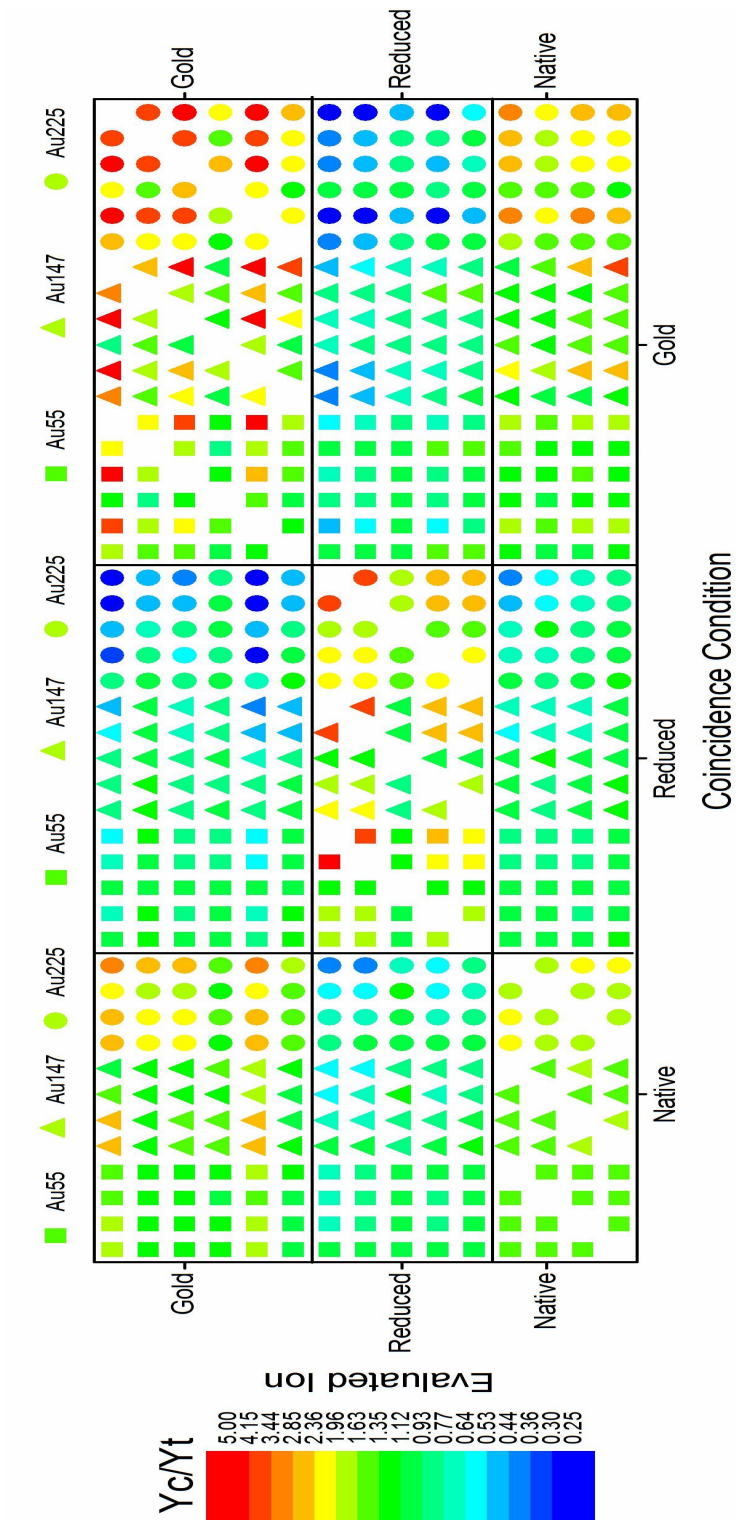
Figure 4.6: Yc/Yt Comparisons Size Dependency

4.4 Summary and Conclusions

This study describes the effect of the size of ultra-small nanoparticles within a nanodomain upon the emission of characteristic ions by bombardment with massive projectiles. Along with the successful detection and analysis of ultra small gold nanoparticles with as few as 55 atoms, we show that for NPs containing between 55 and 225 atoms, there is a linear relationship between their size and SI emission. This suggests a constant ionization probability for ultra-small nanoparticles of the same composition, with overall ion yield dependent upon the number of atoms available within the emission volume of Au_{400}^{4+} . This volume encompasses the entire NP in these ultra-small systems, so all atoms of the NP are sputtered. Due to complete sputtering, differences in impact parameters are not observed. This is a distinction from larger NP systems, where the increased size provides for different types of impacts on the NP and hence non-equivalency of impacts[32]. The data show that the gold nanoparticles preferentially locate within specific chemical environments, namely, in undamaged dendrimer branches. Dendrimer reduction is linked to the size of the nanoparticle, with greater damage seen in larger NP samples. Simultaneously, preferential co-localization of the gold nanoparticle with the native dendrimer structure increases with the size of the nanoparticle, likely due to the greater segregation of native and reduced structures. This example illustrates the feasibility of chemical characterization within 10 nm of individual ultra small nanoparticles, providing information not obtainable by other techniques. Enhanced chemical understanding could lead to increased insight into particle synthesis, in turn facilitating directed growth of nanoparticles within a system by tuning the amount of reductant introduced during synthesis.

41

5. FORMATION OF POLYATOMIC SPECIES FROM HYPERVELOCITY FULLERENE BOMBARDMENT*

5.1   Introduction

The analysis of ejecta arising from hypervelocity impacts has been of interest throughout many disciplines, from planetary science to gas phase physics. Secondary ion mass spectrometry, SIMS, allows for the experimental modeling of these hypervelocity impacts using a wide variety of colliding moieties while also allowing for the control of the kinetic energy deposited in the impact. SIMS experiments using primary ion bombardment of hydrocarbons simulate the impacts of a target surface with a carbonaceous material, such as interstellar impacts with nano dust particles. The mass analysis of the ejected ions yields information about the surface, the interaction between the surface and the impactor, and the possible mechanisms of ionization. Thus, a single instrument can both model these impacts and return ion data to the investigator.

We describe a custom built SIMS instrument operating in the event-by-event bombardment mode that can be used to model carbonaceous impacts on a variety of surfaces. The selection of projectile, charge state, and voltages applied in the acceleration region and on the target allow for the control of the kinetic energy of the projectile and thereby the velocity at impact. Studying a velocity range allows for the simulation of solar impact processes that have previously been observed while also gathering mass spectral data. This makes it possible to identify secondary ions emitted in impacts and can lead to a greater understanding of the mechanism of ionization and emission.

5.2   Source

The carbonaceous impactor source is a custom built device containing a heated reservoir, two pairs of deflectors, and a Wien filter that allows for the selection of the primary ion for bombardment. A copper effusion source is resistively heated up to 700°C to sublime the contained carbonaceous powder. The contained C_{60} escapes through a 250 μm orifice that directs the flow into an ionization region where a Ta cathode (Kimball Physics) is heated and negatively biased to produce (10-150 eV) electrons ionizing the gaseous plume by electron impact ionization. A repelling electrode reflects the electrons back towards the orifice which results in an increase in the cross section of electron- plume interaction. In this study the carbonaceous projectile is isotope ^{13}C labeled C_{60} (80% enriched, MER Corp, Tucson, AZ) is ionized to C_{60}^{q+} (q 1-3) and is accelerated to 10-15 qkV.

An electrostatic lens and a pair of deflectors focus and align the beam into a Wien filter. The Wien filter uses a variable electric field crossed with a permanent magnet in order to mass select charged C_{60} ions with a mass resolution of 7.8 (FWHM 10 kV C_{60}^{+}) which is sufficient to separate the different charge states of $^{13}C_{60}$ (Figure 5.1). A second electrostatic lens and deflector pair focus and steer the selected beam towards the target with a spot size of 10-200 μm. The impact rate is controlled to be less than 2500/s by tuning the current of the Ta cathode, satisfying the requirements for event-by-event bombardment/detection mode in which each individual C_{60} impact is separated in both time and space and recorded individually. Typical analysis is performed with 1-5x10^6 impacts.

5.3   Method

The secondary ions emitted from each impact are recorded separately. A total mass spectrum is obtained by summing all events together. However, since emitted
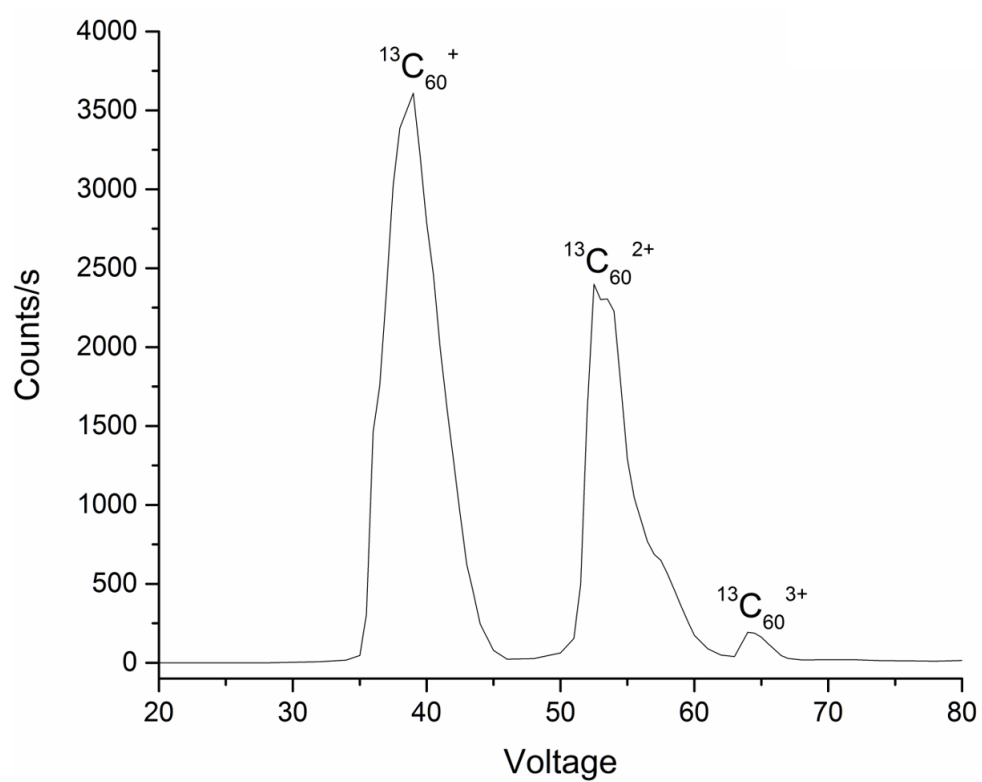
Figure 5.1: Wien Filter Scan

secondary ions are paired with an impact it is possible to select ions of interest and sum a subset of impacts where those ions were detected. This is termed a coincidental spectrum as the observed ions must be coincidentally emitted during impacts where the ion of interest is observed[38]. The area of emission of secondary ions is approximately 10 nm in diameter, thus any co-emitted ions must be collocated within this area. This means that each impact is truly a nanometric probe useful in the characterization of surfaces at the nanoscale. Ions produced show chemistry occurring under these constrained, non-equilibrium conditions and hence provides insight into processes occurring between the surface and projectile.

The event-by-event bombardment mode amounts to stochastic sampling. With a bombardment zone of 200 μm in diameter and sputtering diameter of <6 nm^2 per impact then less than $1x10^{-4}$% of the surface will have been analyzed[39]. Running in this "super static" regime the probability of impacting an already sampled region is low.

The impact velocities with C$_{60}$ or ^{13}C$_{60}$ ranged between 70 and 142 km/s. Studies on the effects of impact velocity were carried out on the same day to ensure that instrumental tuning and response are consistant. Other impactors could conceivably be utilized in the future, with the requirement that their sublimation point is below the maximum heating provided by the copper heater. Such projectiles could be amino acids and peptides, as most have a sublimation temperature below 300°C [40]. The larger masses of such projectiles would allow for lower impact velocities for future studies.

5.4 Sample Preparation

5.4.1 Powders

A custom sample holder was designed for the analysis of powder samples. The holder consists of four parts; a stainless steel body that contains the powder sample, a 90% transmission nickel grid which eliminates surface charging, a stainless steel collar that mates the grid to the body through a friction connection, and a stainless steel plug that is used to compact and secure the powder using a set screw. This sample holder allows for the direct analysis of small amounts of powdered samples, less than $\sim$100 mg, and reduces effects due to sample charging or height differences in the mass spectra. The holder can also be easily dissassembled for cleaning.

The analysis of CsI shows a conventional mass spectrum similar to those present in the literature can be obtained for samples prepared either by vapor deposition or by utilizing our custom powder holder. Both spectra show characteristic cluster ions. The powder sample shows an increase in emission of CsI clusters, since there can be no contribution from the support and a mono crystal structure is produced during sample preparation. In pressing the CsI powder under a 5 ton hydraulic press the resulting pellet produced is semi-transparent and $\sim$1 mm thick, suggesting that a single crystal was produced.

5.4.2 Vapor Deposition

The production of a flat, micron-thick layer of sample on a Si wafer was achieved in vacuum ($\sim 10^{-3}$ Torr) through resistively heating an aluminum assembly containing powdered samples. Single to multi layer depositions can be obtained by varying the deposition time.

Table 5.1: Characteristic Ion Yields for Powder and Vapor Deposited CsI Samples

Ion	Compressed Powder CsI		Vapor Deposited CsI	
	79 km/s $^{13}C_{60}$	111km/s $^{13}C_{60}$	79 km/s $^{13}C_{60}$	111km/s $^{13}C_{60}$
I^-	0.31	0.54	0.15	0.21
$(CsI)I^-$	0.36	0.57	0.12	0.21
$(CsI)_2I^-$	0.075	0.16	0.021	0.046
$(CsI)_3I^-$	0.027	0.040	$4.3x10^{-3}$	0.011
$(CsI)_4I^-$	$9.5x10^{-3}$	0.015	$1.5x10^{-3}$	$3.4x10^{-3}$
$(CsI)_5I^-$	$2.4x10^{-3}$	$4.8x10^{-3}$	$2.7x10^{-4}$	$8.5x10^{-4}$
$(CsI)_6I^-$	$1.7x10^{-3}$	$3.1x10^{-3}$	ND	ND

5.5   Results

5.5.1   Cesium Iodide

Table 5.1 lists the yields for characteristic ions for both samples bombarded with $^{13}C_{60}$, calculated using Eq. 2.17. This shows that ion emission is preferred in the powder sample compared with the vapor deposited CsI. Larger clusters are observed when bombarding the powder and yields of all characteristic ions are enhanced by 2-10x.

This enhancement is likely due to microscopic surface roughness versus the well defined atomic layers produced from vapor condensation. A larger surface area facilitates the emission of secondary ions.

5.5.2   Sodium Nitrate

The analysis of sodium nitrate was performed due to its abundance as an astronomical mineral that can undergo micrometeorite impacts. Here, the powder coats the grid and so two different heights are observed in the spectra, as evidenced by peak splitting. Coincidental analysis allows for the exclusion of peaks either from the support in the case of the vapor deposition sample or from the nickel grid in the

case of the powder sample. By selecting the NO_3 peak as a coincidental condition and summing only impacts where this ion was observed, it is possible to select a subset of data where bombardment on the pristine sample surface occurred. Total yield is calculated using Equation 2.17, where the intensity of an ion A is divided by the total number of impacts. Equation 2.19 describes the coincidental yield, where the intensity of an ion of interest, A, in coincidence with another ion of interest, B, is divided by the number of impacts where ion B is emitted. Effectively, the coincidental yield gives the probability of observing an ion emitted in an event with another specified ion.

Figure 5.2 shows the qualitative differences between spectra based on the coincidental condition applied. Figure 5.2a shows the total mass spectrum is observed of a powder $NaNO_3$ sample bombarded by 116 km/s C_{60} projectiles. Characteristic peaks arising from the nitrate moiety and from emitted ion clusters are observed. Contributions from different sample heights and the grid appear as split peaks when ions produced closer to the extraction grid spend less time in the field free region and arrive before ions produced in the sample depths. When a coincidental condition is applied to the data which selects impacts of the C_{60} on the grid and high topographic areas of the sample, the splitting of the peaks is reduced and a time shift is observed to shorter times (Figure 5.2b). By setting a coincidental condition on the NO_3 peak, it is possible to select impacts on the powder sample and exclude impacts on the grid. Here we see that the peak splitting is again removed and that a clean spectrum of $NaNO_3$ is produced (Figure 5.2c).

The CN^- is not present in the sample and hence must be produced during the impact. Previous studies have shown CN^- production from organic samples[41], here we report the recombination observed in an inorganic target.
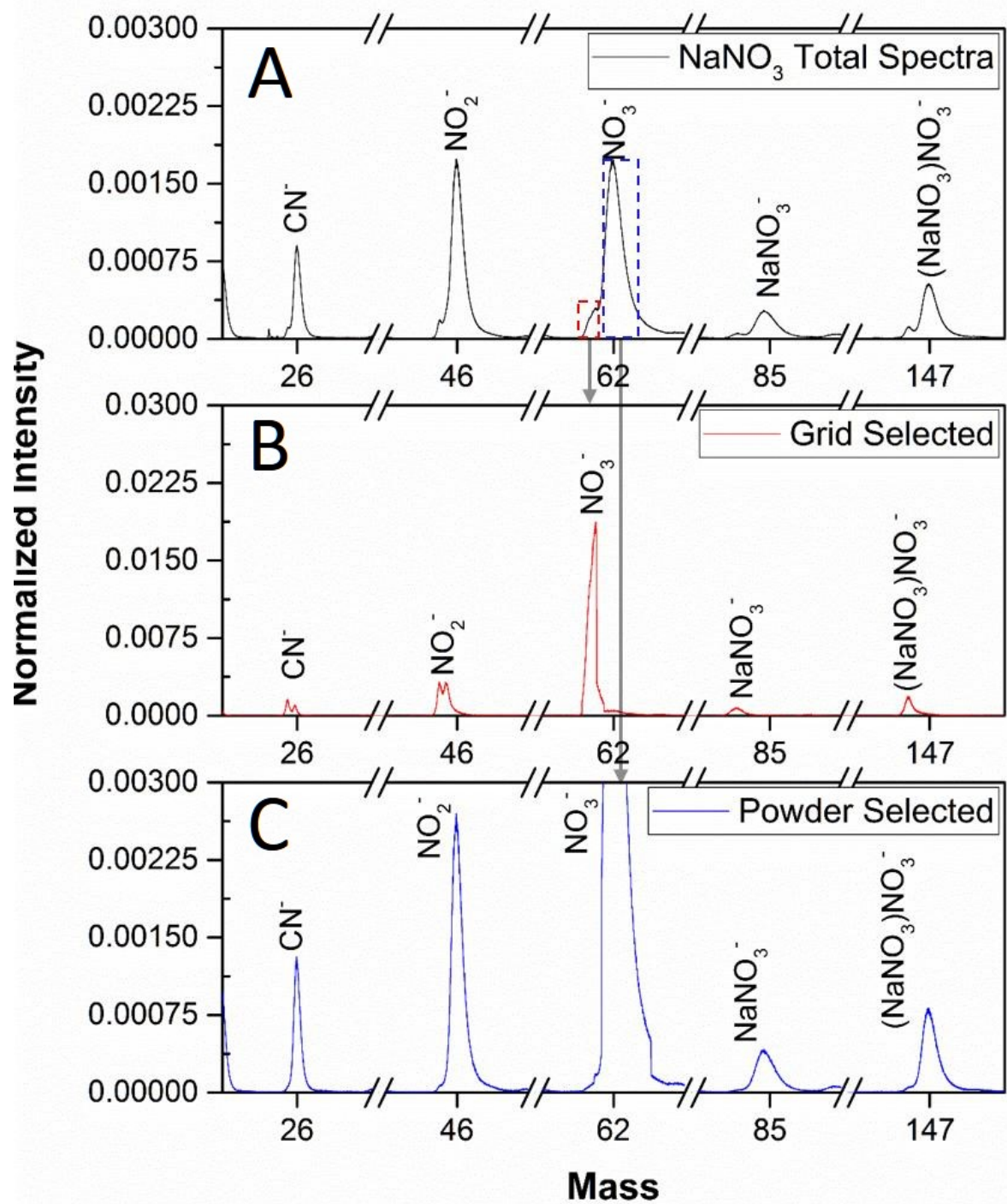
Figure 5.2: Selection of Impacts on Grid or Powder Through Coincidental Analysis

5.5.3 Ammonium Nitrate

Ammonium nitrate was bombarded by labeled $^{13}C_{60}$ projectiles to simulate the impacts of cabonaceous impactors in interstellar space. The use of isotopically labeled C_{60} allows for the determination of the source of carbon within produced ions. ^{12}C is present as surface contamination on the sample and ^{13}C is delivered by the impactor. Two impact velocties are shown in Figure 5.3 where increased energies again show enhancement of ion signal. Crucially, carbon and nitrogen recombination peaks are again observed showing interaction of the projectile and sample surface.

The oxidation state of atoms in the sample could be expected to play a role in the formation of important recombination ions, where the nitrogen is available from either the amine or the nitrate moities of ammonium nitrate. To elucidate if any preference arises from the oxidation state of the nitrogen, isotopically labeled ammonium nitrate samples were analyzed ($^{15}NH_4NO_3$ and $NH_4^{15}NO_3$, Cambridge Isotope Labs, I-15868, I-16323). The lack of a peak at m/z 28 (Figure 5.3, inset) allows for the analysis of projectile-sample recombination to form $^{13}C^{15}N$.

The data were again analyzed by placing a coincidental condition on the characteristic NO_3^- peak so that only impacts on the sample were used for analysis. Figure 5.4 shows coincidental ion yields of recombination and nitrate ions under this coincidental condition (Table of numerical values provided in Appendix C). The coincidental yields for $^{14}NH_4$ and $^{15}NO_3$ containing samples are shown to be consistent, suggesting that there is no memory effect since both nitrogen moities equally participate in the recombination process regardless of their original oxidation state.
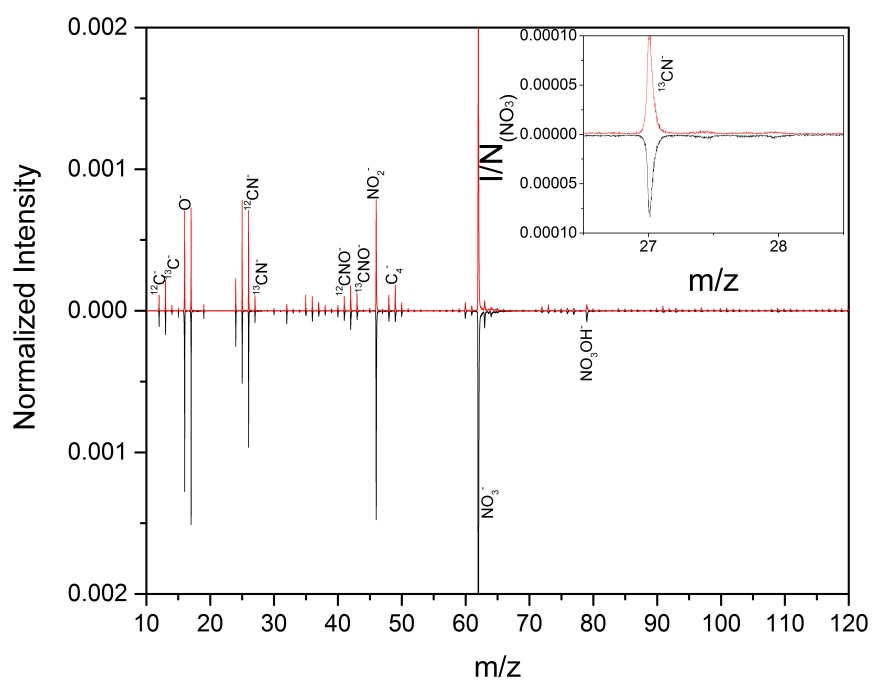
Figure 5.3: Mass Spectrum of NH_4NO_3 at 79 km/s Impact Velocity (Red) and 111 km/s (Black)
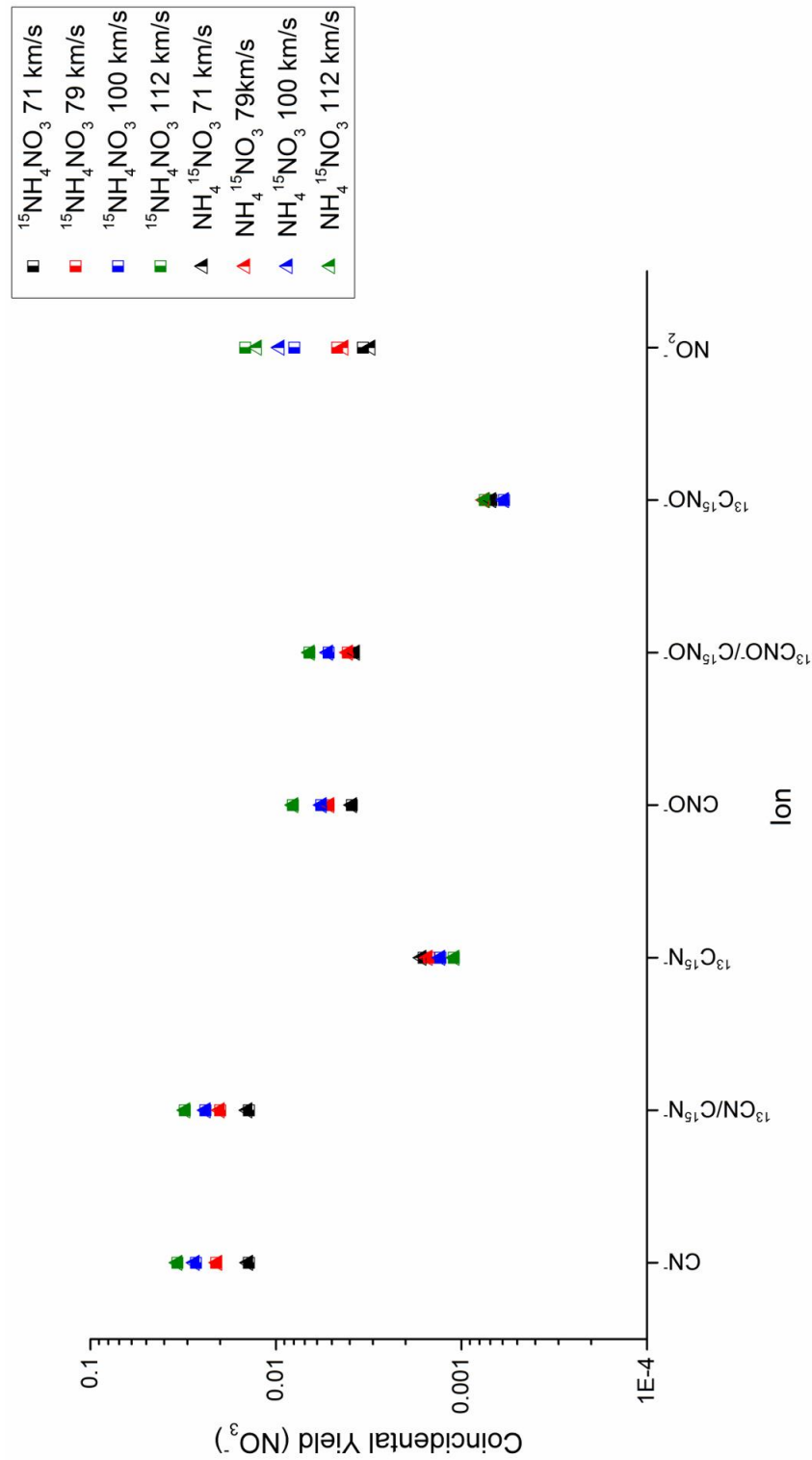
Figure 5.4: Coincidental Yield of Relevant Ions at Different Impact Velocities.

Figure 5.4 also shows that the coincidental yield of recombination arising solely from projectile-sample interactions ($^{13}C^{15}N$) shows an interesting trend. It is observed that increasing the impact velocity causes a decrease in the yield (Figure 5.5). Here, carbon from the projectile is embedded into the surface during the impacts, with higher impact velocites resulting in deeper penetration therefore subsequently lowering the sputtered ^{13}C. These isobaric peaks are dominated by ^{12}C recombination ions instead of projectile-sample recombination.

CN and CNO have increasing yields due to the increasing sputter volume as impact velocity increases, and the same trend is seen for peaks at m/z 27 and 43. These peaks arise from the recombination of labeled nitrogen with contaminate ^{12}C ($^{12}C^{15}N$ and $^{12}C^{15}NO$). Isobaric interferences with $^{13}C^{14}N$ and $^{13}C^{14}NO$ are less likely due to the lack of nitrogen contamination to provide a ready source for interaction and so are expected to be minor contribitors.

Other non-recombination products also show an increasing yield as the impact velocity increases due to the increased sputtering volume, shown most notably by the increased coincidental yield of NO_2.
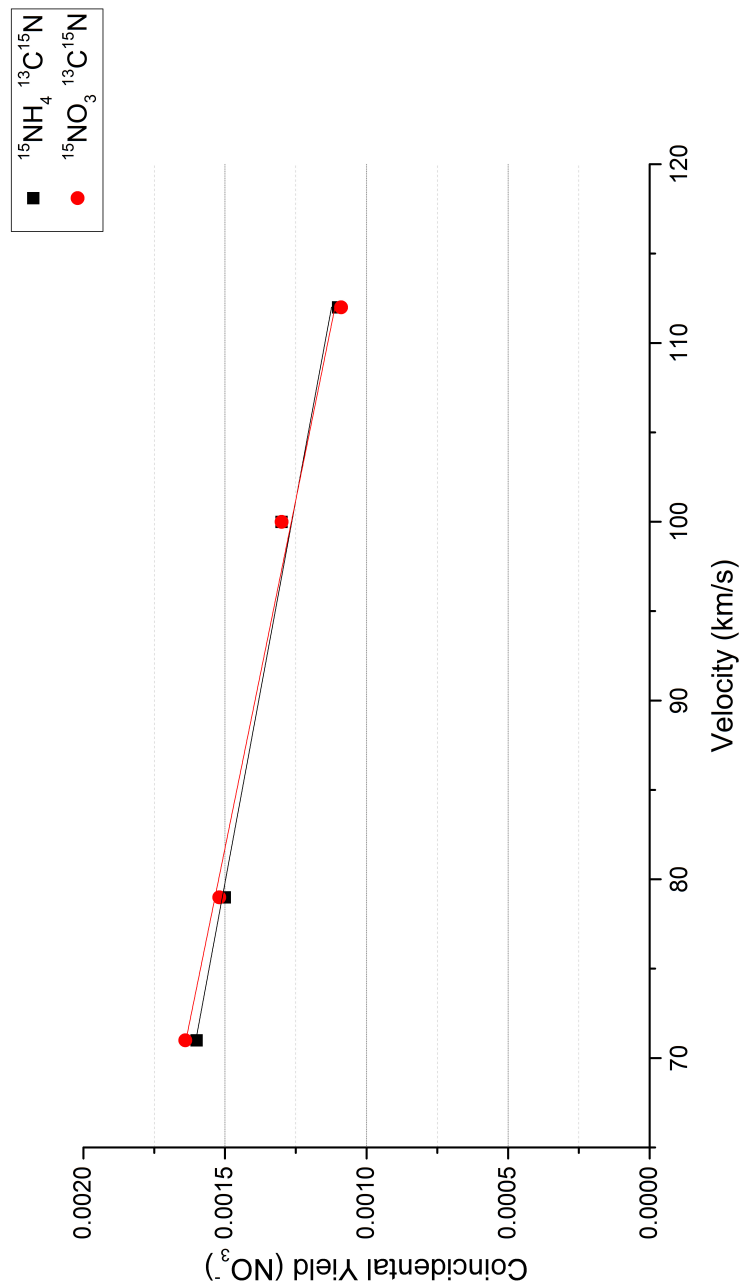
Figure 5.5: Coincidental Yield of $^{13}C^{15}N$ Recombination Ion at Increasing Impact Velocities for Isotope Labeled Ammonium Nitrates.

The recombination ion $^{13}C^{15}NO$ shows no increase in yield as impact velocity increases, suggesting that the yields are limited by the amount of labeled ^{13}C that can be delivered per impact. Figure 5.6 shows this trend, where recombination of three atoms is statistically less likely than the recombination of two atoms. When coupled to the low counting statistics arising from these low yield ions, an increasing contribution from background signal could possibly masks any impact velocity trends.
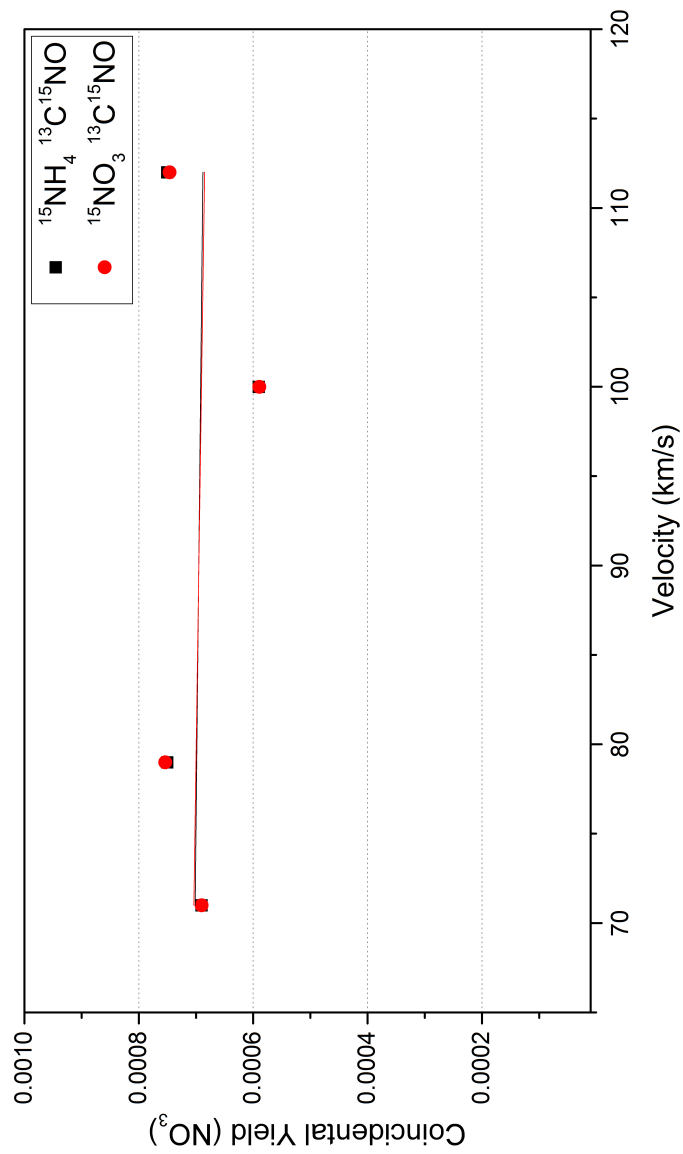
Figure 5.6: Coincidental Yield of $^{13}C^{15}NO$ Recombination Ion at Increasing Impact Velocities for Isotope Labeled Ammonium Nitrates.

The coincidental yields for all three CNO moieties support the hypothesis that they are created from a three atom recombination process and not from an interaction of carbon with pre-formed NO from the sample. Yields are the same for these species regardless of the position of the isotope labeled nitrogen. If pre-formed NO on the surface was recombining with carbon then a difference in yield would be expected, especially for the $^{13}C^{15}NO$ peak which should not be present during analysis of a $^{15}NH_4NO_3$ sample.

5.6   Conclusions

Currently, experimental modeling exists using either larger (micron) dust particle impactors or by approximation using laser pulses[42]. Our technique can extend the study of impacts started by dust impactors down to the nanometer scale as well as providing a separate model to compare data produced from laser pulse studies.

These first studies show that bombardment of a native powder results in the emission of larger and more abundant cluster ions from CsI. This is due to a larger emission area, due to the surface roughness, which increases the overall yield. This result has the added benefit of not requiring chemically or thermally destructive sample preparation techniques, preserving the original sample state.

The production of organic recombination ions from inorganic samples with carbon delivered by a carbonaceous impactor is also observed. The use of isotope labeled projectiles allows for the identification of recombinations either with surface carbon or that delivered in the projectile. The recombination yield of species containing carbon from contamination show increasing sputter rates as impact velocity is increased, similar to the increased sputtering observed for analyte specific ions. Crucially, recombination yields for ions produced with delivered carbon from the impactor show decreasing yields as the projectile embeds within the surface which reduces emission

of delivered, labeled carbon, such is the case with $^{13}C^{15}N$, or no trend is observed for recombination as impact energies are varied ($^{13}C^{15}NO$). TRIM (Transport of Ions in Matter) calculations show a ^{13}C range of between 2-3.5 nm for impact velocities of 70-111 km/s. Previous studies have shown that the range of a C_{60} cluster to be 50% deeper than a carbon atom with the same energy per atom[43]. Thus, a predicted projectile range of 3-5 nm for impact velocities between 70-111 km/s could prevent to re-emission of ^{13}C from the projectile. The lack of energy dependence also suggests that in the more complicated three body recombination the delivered ^{13}C acts as a limiting reagent so increased sputtering does not result in increased ion production.

The versatility of event-by-event bombardment is illustrated through the ability to probe individual carbonaceous impacts on a surface via the coincidental mass spectrometry technique. This coincidental methodology allows for the selection of subsets of impacts where an impact occurs on a pristine sample which removes interferences from height differences, grids, or underlying supports. Thus, only interactions between the carbonaceous impactor and the sample of choice are studied. Future studies should focus on the use of more massive projectiles to bring the impact velocities closer in line with those observed in space, where typical velocities are around 20 km/s[44].

6. NANOPARTICLE IMPACTS ON FREE STANDING GRAPHENE*

6.1 Introduction

While extensive studies have been performed on the interaction of nanoparticle projectiles with 3D matter with regards to surface damage, modification, implantation, and sputtering[45, 46, 47, 48], few studies have dealt with interactions of bombardment of 2D materials. In a confined system transfer of energy through a collision cascade is impossible, and so must undergo a different process of sputtering. This chapter describes the emission of carbon from free standing graphene sheets bombarded by individual Au_{400}^{4+} projectiles. Collection of secondary ions in both the transmission and reflection direction after bombardment allows for insight into the sputtering process through preferential emission in certain directions. The event-by-event bombardment/detection mode allows for the study of individual impacts and for the analysis of free-standing graphene without an underlying support structure[49].

The interaction of suspended graphene with energetic ions or clusters has previously only been simulated using molecular dynamics. These studies have focused primarily on the physical properties of graphene, such as penetration resistance and deformation[50, 51, 52, 53]. Other simulations have studied the formation of holes produced in free standing graphene due to atomic or cluster bombardment[54, 55]. Massive clusters in the energy range studied here deposit energy into bulk material through a hydrodynamic flow and travel in a cohesive manner through the target[56]. For film or graphene targets, the confined dimensions allow for the exit of the pro-

jectile. Previous studies on carbon films between 5-20 nm have shown that the Au_{400}^{4+} projectile pushes matter out of the target, causing abundant emission of secondary ions in the transmission direction [57]. The distribution and yield of emitted carbon clusters greatly varies between the transmission and reflection direction. It was also shown that the projectile is fragmented upon exiting a 5 nm carbon foil. Using graphene as a 2D target, a different interaction occurs. In the following this graphene case is compared with carbon foils to determine a possible emission process.

6.2   Experimental

Graphene was bombarded using the Au_{400}^{4+} instrument described in Chapter 2. A new analysis chamber was constructed utilizing two identical 60 cm linear time of flight mass spectrometers for secondary ion characterization with an 8 anode detector. An electron detection leg was also used on both sides to provide a start signal from electrons deviated with an electromagnet. The Au_{400}^{4+} beam was passed through the analysis chamber previously detailed and was refocused using an Einzel lens between the two chambers. Bombardment of free standing graphene targets was carried out at 30 degrees.
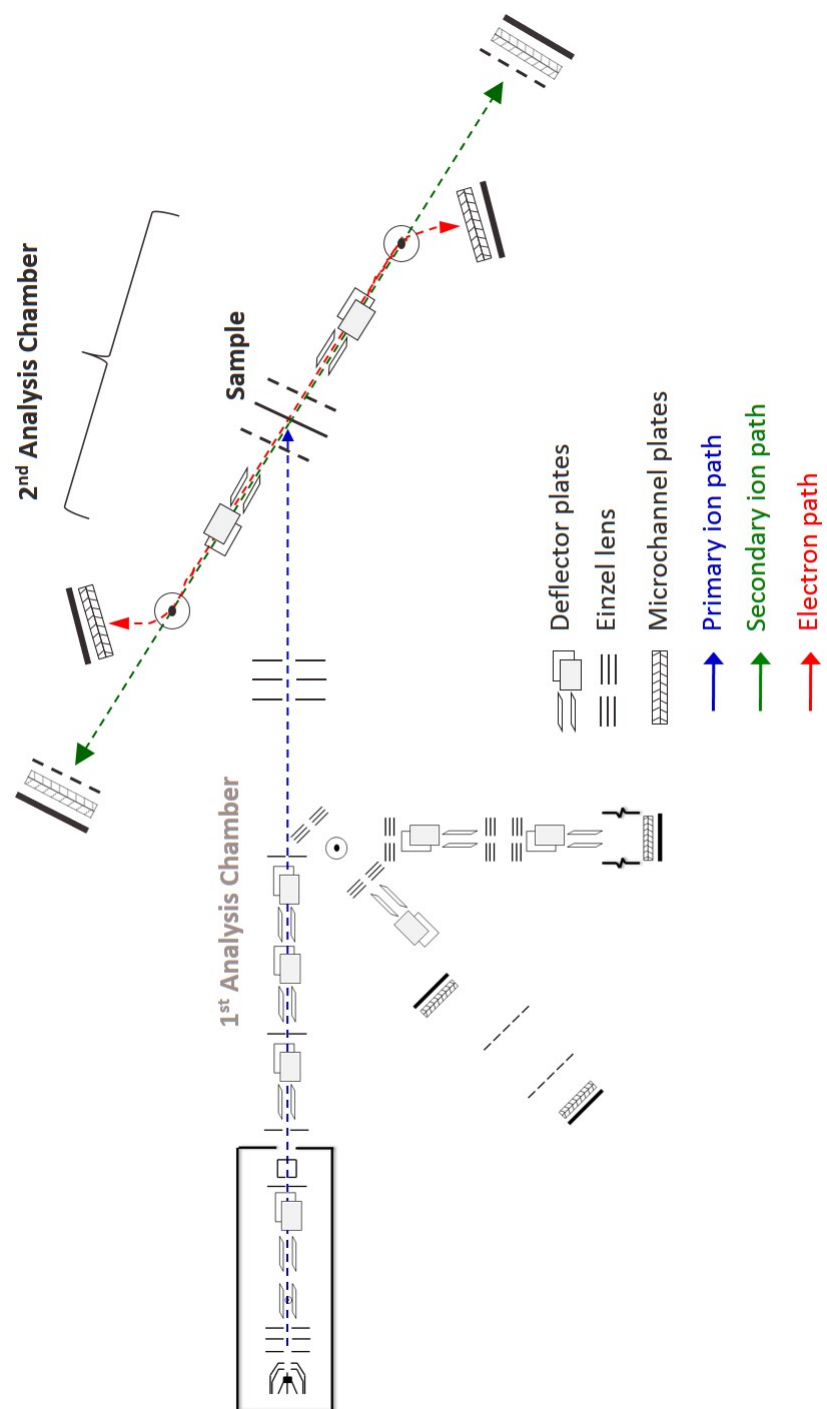
Figure 6.1: Instrument Schematic for Dual ToF Analysis of Free Standing Graphene

6.2.1 Graphene Characterization

The graphene targets consist of a graphene film supported by a lacey carbon film on a 300 line per inch copper TEM grid (Ted Pella, Inc., Redding, CA). The purity of the graphene was analyzed using micro-raman spectroscopy to verify that pristine layers were utilized in this study and to confirm the number of graphene layers on the sample. TEM and SEM micrographs were obtained to verify the lack of defects or holes within the sample structure as well.
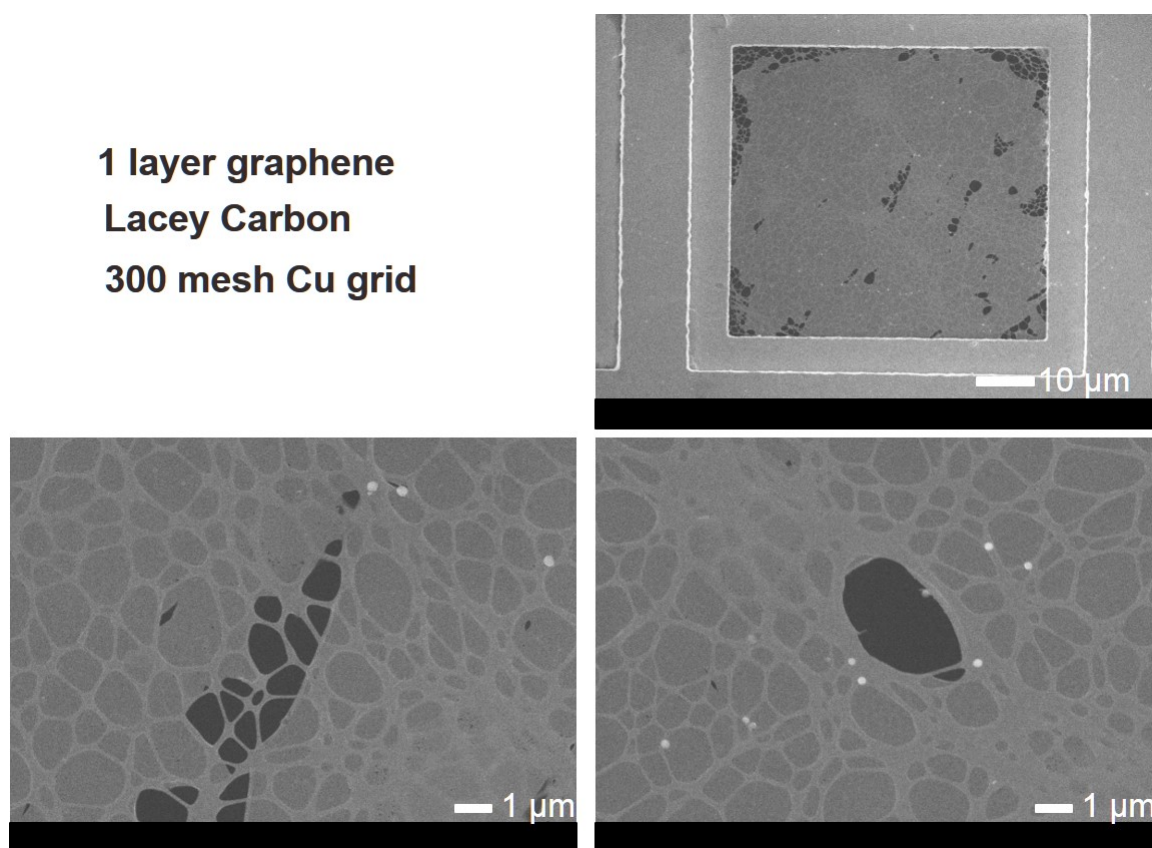
Figure 6.2: TEM Micrographs of Graphene Target Showing Lacey Carbon and Copper Support

The lacey carbon support is reported to be ∼100 nm in diameter. Due to this large thickness, direct impacts on the lacey carbon do not cause emission in the transmission direction. However, grazing impacts on the lacey carbon, impacts which strike the edge, can result in ion emission. It was found that the yield of carbon clusters from samples of lacey carbon normalized to all impacts on the surface (by transmission) was on average ∼84 times lower than that measured from impacts on single layer graphene. Moreover the distribution of the carbon clusters is different from that observed with single layer graphene. We therefore conclude that the contribution of grazing impacts on the observed mass spectra from the graphene samples is negligible.

Raman spectroscopy was used to verify the number of graphene layers in the samples so that thickness comparisons could be made. The characteristic 2D and G bands are prominant in the spectra and the wavenumber shift can be used to determine number of layers present[58]. Figure 6.3 shows the specta of single layer graphene with a G band at 1594.9 cm^{-1} and a 2D band at 2646.4 cm^{-1}. Figure 6.4 shows a four layer graphene target where the G band is shifted to 1582.6 cm^{-1} while the 2D band remains effectively unchanged at 2647.7 cm^{-1}. Thus, the G band can be utilized to determine layer thickness, as has been previously reported.
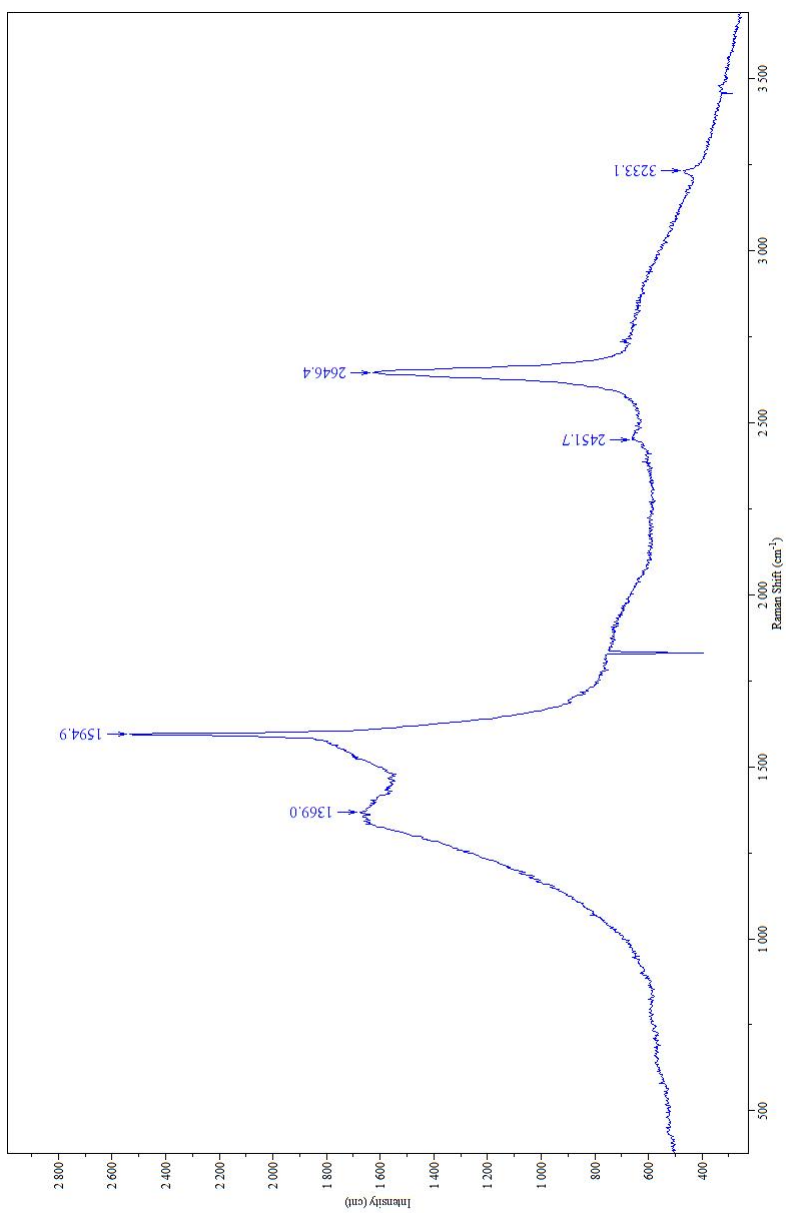
Figure 6.3: Raman Spectrum of Single Layer Graphene
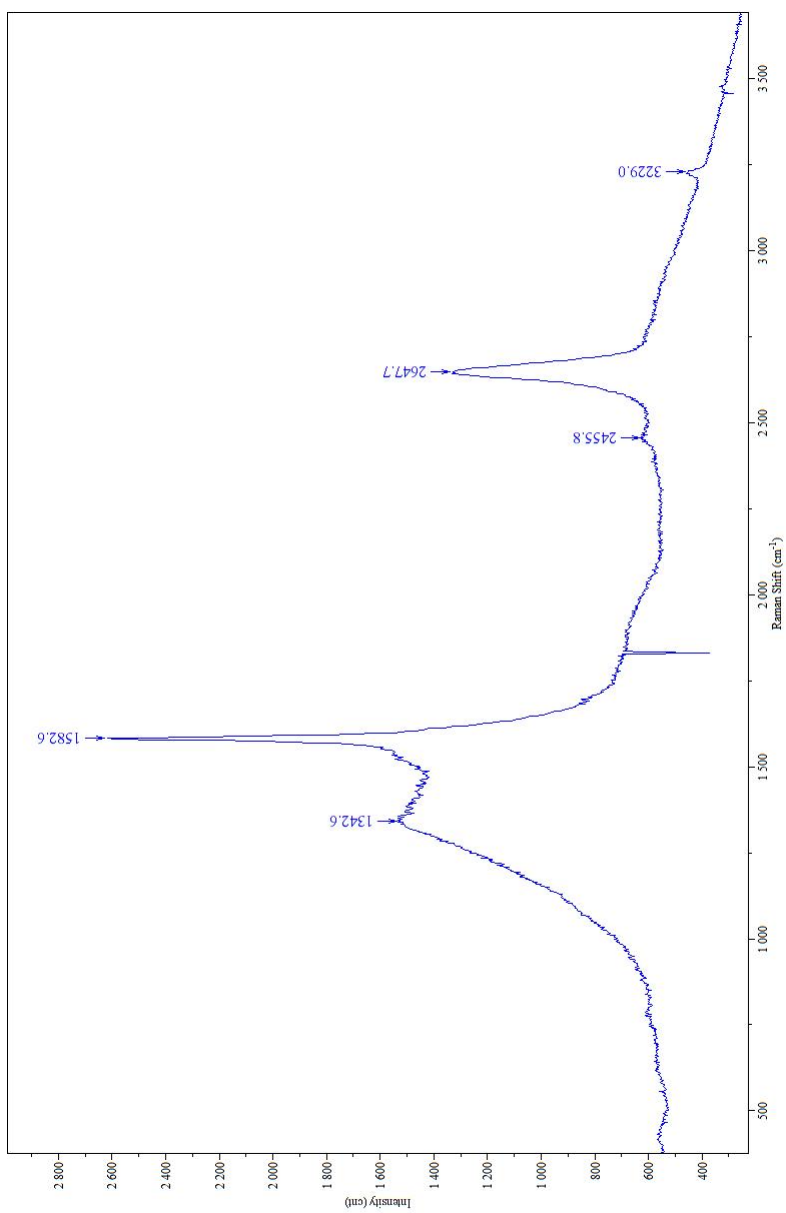
Figure 6.4: Raman Spectrum of Four Layer Graphene

In the spectra, large background contributions can be seen. This is due to the amorphous carbon from the lacey carbon support, and results in the broad D peak seen around 1370 cm^{-1}.

6.3 Results

After bombardment, TEM microscopy detailed the production of large holes in the graphene sample. These round holes are characterized by the observance of a rim structure and by their much larger size than the Au_{400}^{4+} projectile. The Au_{400}^{4+} projectile is $\sim$ 2 nm in diameter, so it is surprising to find that the produced holes are between 8-9 nm. Holes produced on a 5 nm carbon film are 15 nm in diameter which is consistent with values previously reported. The production of such large holes is unexpected, given that the 2D confinement of the graphene prevents a collision cascade that could deposit energy over a larger volume. It is also crucial to note that molecular dynamic simulations do not predict such a large hole on graphene, instead modeling a hole size 50% larger than the diameter of the incident projectile[55].

6.3.1 Secondary Ion Emission

Negative ions produced from bombardment of graphene are characterized by a range of carbon clusters C_n^-, C_nH^-, $C_nH_2^-$). H^-, O^-, and OH^- are also produced from either an absorbed contaminate layer or from oxidized graphene sections. $Cu_xCl_y^-$ clusters are also observed from bombardment of copper chloride nanoparticles that remain from the manufacturing process. Positive ions observed include H_n^-, C_n^+, C_n^+, $C_nH_2^+$, Cu_n^+, Na_n^+, and K_n^+. The emission of carbon clusters from the lacy carbon support was determined to be negligible as position of the support structure either before or after the graphene with respect to the incident beam did not affect the mass spectra obtained.

The yields of carbon clusters are presented in Figure 6.6. Small clusters dominate
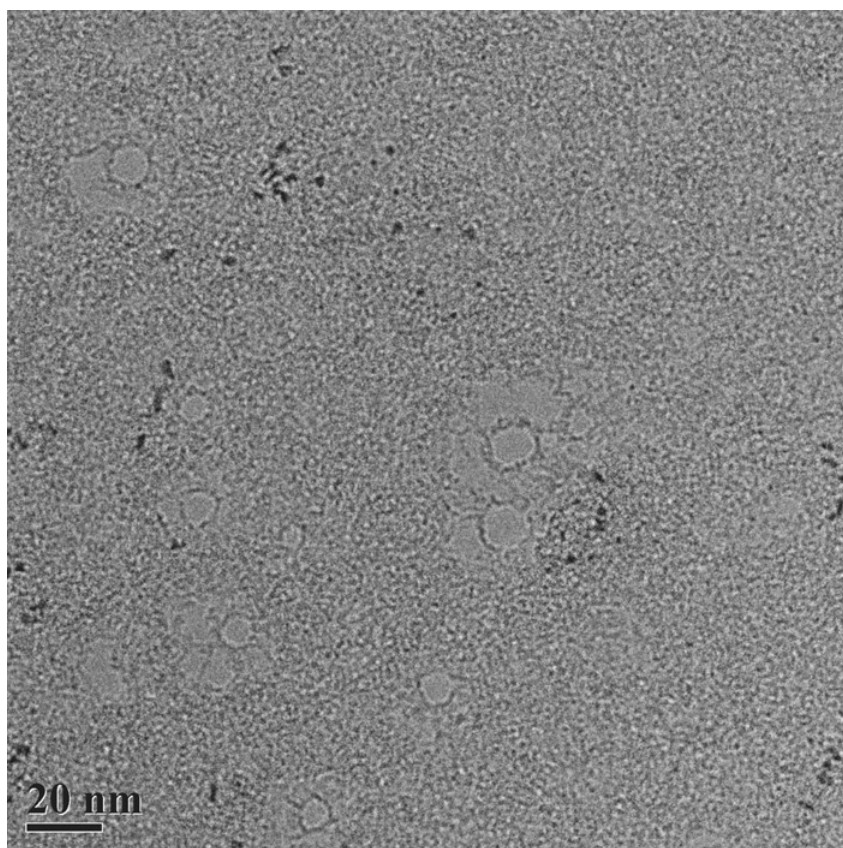
Figure 6.5: TEM Micrographs Holes Produced in Single Layer Graphene After Bombardment

the spectra as emission of increasingly large carbon clusters is not preferential to further fragmentation. An odd-even oscillation is observed with preferential emission of even numbered clusters being observed as negative ions. This has been observed previously in carbon films as well as in bulk samples[57, 59].
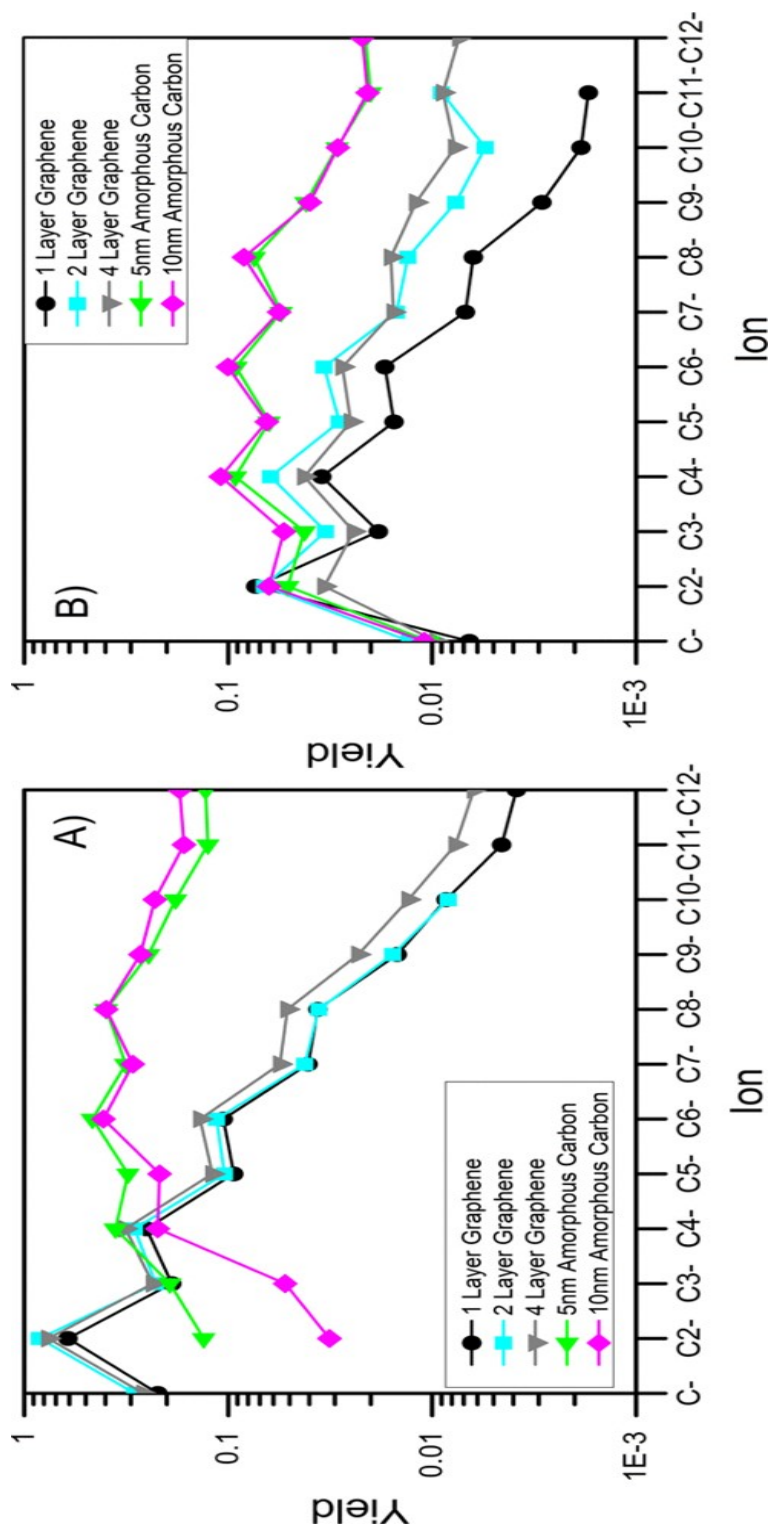
Figure 6.6: Yields of Carbon Clusters in (A) Transmission and (B) Reflection Directions

The transmission direction shows an independence of cluster yield with regards to the thickness of the graphene target. Single, double, and quadruple layer graphene targets have similar yields, but are drastically different from the bulk cases shown in 5 or 10 nm carbon films. These trends are repeated for clusters of C_nH^- and $C_nH_2^-$ but their overall yields are reduced from the C_n^- clusters.

In the reflection direction, secondary ions are emitted from all samples which is surprising considering the small interaction volume and the momentum pulse delivered by the Au_{400}^{4+} projectile in the opposite direction. The emission of clusters in the reflection direction is characterized by nearly an order of magnitude decrease in yield over transmission yields, up to 10-50x lower. The distribution of ions is also markedly different in the two cases, with the reflection direction being much broader. A small layer thickness dependence is also observed with a greater yield of large C_n^- clusters over the 2 or 1 layer graphene targets, where clusters above C_3^- have a yield 2-3x higher. At the same time a reduction of small C_n^- cluster emission is also seen. For single and double layer graphene, C_2^- is the dominate cluster emitted but for 4 layer graphene C_4^- is the most prominent.

In the reflection direction, graphene behaves similarly to bulk materials in the distribution of carbon clusters. This suggests that the emission processes for backwards emitted clusters is consistent in 2D and 3D materials. Reflected ejecta from graphene and carbon films must originate from an area surrounding the impact zone as all material directly in the target-projectile interface must be knocked on in the transmission direction as a consequence of the momentum transfer involved.

Comparing the graphene to the carbon foil targets, the shift from 2D to 3D emission processes are evident. Cluster emission from carbon foils show no thickness dependence, and are much more likely to have emission of large clusters up to C_{12}^-. This is due to the increased matter available for sputtering. It is possible to estimate

the number of ejected carbon atoms using the hole diameter as measured by TEM. For single layer graphene, $\sim 3x10^3$ carbon atoms are ejected. Summing the carbon ions emitted in both directions give an ionized fraction of the ejected carbon is 0.01, which is a higher fraction than would be expected from molecular dynamic simulations and studies on bulk materials.

In positive ion mode, carbon emission of odd numbered clusters dominate which is expected from previous studies[60, 61, 62, 63, 64]. Again, it is observed that transmission ions are at least ten times more abundant than in the reflection direction. Low mass species dominate the graphene spectra. The emission of H_n^+ and C^+ indicate a high charge around the hole produced during the impact. These species have also been shown previously to emit promptly ($\sim 10^{-15}$s) under bombardment with MeV projectiles. A high charge is observed due to the passage of the projectile[65, 66, 67]. The large increase in C^+ yield in the transmission direction over the reflection direction is again due to the high kinetic secondary ions emitted in the same direction as the projectile.
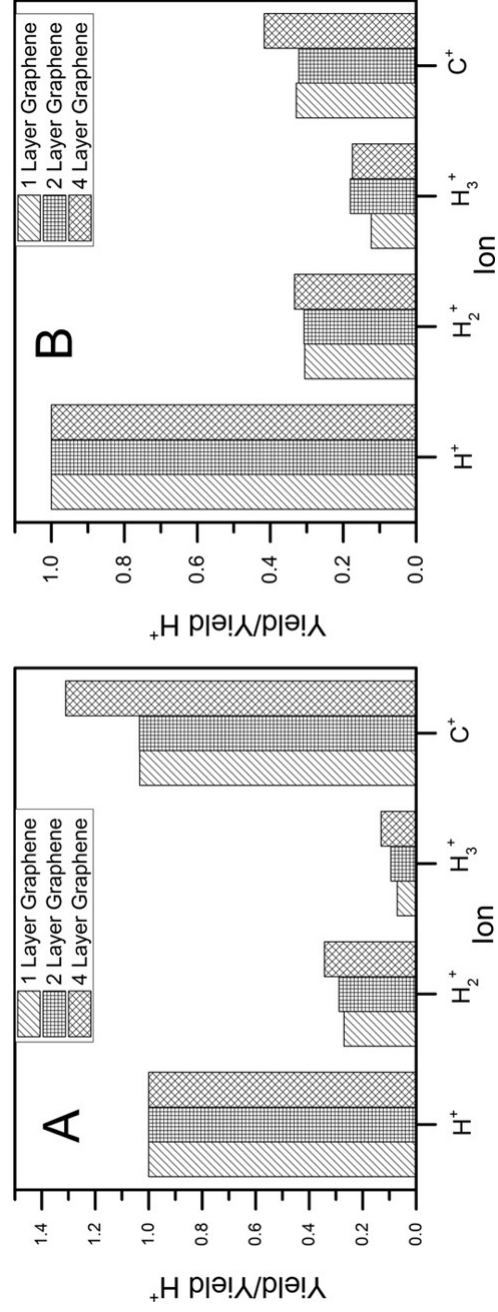
Figure 6.7: Positive Hydrogen Clusters and C^+ Yields, Normalized to H^+ in the (A) Transmission and (B) Reflection Directions

6.3.2   Hole Production and Emission of Ions

As mentioned previously, the size of the produced holes in graphene is much larger than that of the impacting projectile. A region outside the direct impact zone must have energy deposited within it and then undergo sputtering. This is evidenced in the spectra as small carbon cluster peaks result from two processes. A high velocity shoulder is observed in these peaks from clusters emitted during the direct impact of the Au_{400}^{4+} projectile with the graphene sheet. A momentum pulse sputters carbon clusters and the high energy deposited makes the observation of large carbon clusters unlikely as they will fragment to smaller clusters. A second, lower velocity emission process can also be observed in these peaks. Here, ions are emitted outside of the zone of direct projectile impact and do not obtain extra velocity besides that provided by the extraction field. Thus, these ions arrive at the detector later and the peak splitting observed in the peaks is observed. These slower ions must be emitted from the rim of the projectile-graphene impact zone and are only observed in the transmission direction. A third emission process results in the emission of low velocity clusters due to high charge states created in the interaction zone. From here, H_n^+ (n 1-3) and C^+ are observed in both reflection and transmission directions as the momentum pulse from the projectile is not involved in their emission and so does not force a preferential emission direction. It is also possible that the relaxation of damaged graphene around the initial hole causes the emission of carbon clusters up to C_{12} in both directions. This process provides the majority of the larger carbon clusters ($C_n > 6$) as an inflection is noted in the secondary ion yield of carbon clusters.
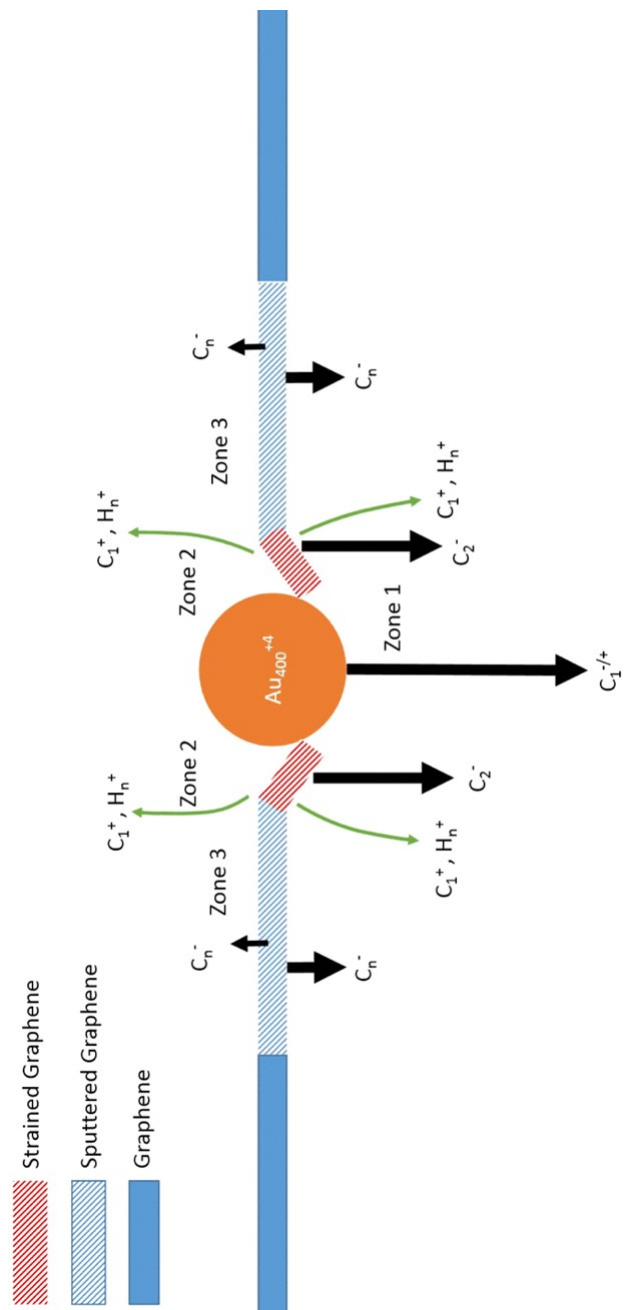
Figure 6.8: Emission Zones of Carbon Clusters from Graphene

The collision of the Au_{400}^{4+} projectile with single layer graphene can be modeled using Stopping Range in Matter (SRIM)[68] software by bombarding a gold target with 73 eV carbon atoms. Using this method it is possible to calculate the fate of the carbon during an impact. It is seen that 65% of the carbon atoms are backscattered, 20% implant within the gold target, and the remaining 15% are transmitted. This agrees with the experimental data that show much higher yields in the transmission direction where carbon atoms and clusters ricochet off the Au_{400}^{4+} projectile.

Because the size of the holes produced is shown to be independent of the number of graphene layers, the deposited energy does not affect the final state of the graphene. Thus, the size of the hole must be dependent on the evolution of stress in the graphene. During bombardment, the graphene first deforms in the direction of the nanoparticle trajectory. Once the projectile penetrates the graphene this stress is released through vibration of the graphene sheet and by the propagation of tears originating in the impact zone. It has been shown in the literature that graphene tears grow in a zigzag or armchair direction of the film[69]. Multiple tears are expected per hole due to the large number of broken bonds around the hole perimeter. These tear will radiate outward and as they propagate and cross it may be possible for large carbon clusters to be emitted as large portions of the graphene are separated by these tears.

The high energy rim around the hole also can be expected to play a role in the emission of carbon clusters. Here, dangling bonds will try to reorient to form a lower energy structure and C-C bonds can be broken in order to obtain a lower energy state[70]. This process will also occur along the edges of tears within the graphene. The ejection of clusters from this process will have no directional preference, and so clusters will be observed in both directions.

Simulations suggests that during the tear process, these sections are pulled toward

the original strain of the projectile. This is validated by the preferential transmission emission seen in the experimental data.

6.4   Conclusions

The interaction of 2D and 3D materials with a hypervelocity Au NP is shown to be markedly different. Experimental evidence support the hypothesis of at least four emission processes for secondary ions in two directions without the presence of a collision cascade. First, direct interaction of the projectile with a graphene target creates small carbon clusters with high velocity in the transmission direction. Second, high velocity secondary ions are emitted from the rim of the produced hole. Third, a high charge state around the perimeter of the hole causes emission of H_n^+ and C^+ in both directions. The origin of this high charge state has yet to be determined. Finally, low velocity carbon clusters are emitted through the propagation of tears and the hole in the graphene sheets. Dual direction detection allows for the analysis of these processes through secondary ion yields and peak shape investigation.

The high percentage of ionized carbon atoms ($\sim 1\%$) is also very interesting. Most of these emitted ions are observed in the transmission direction due to the momentum pulse of the projectile. Ion emission seems to be largely independent of sample thickness suggesting that the majority of emitted ions originate from the outermost graphene layers. Finally, the observed hole size after bombardment is considerably larger than the projectile used in the bombardment. This suggests a new process of ion emission that is largely dependent on propagation of tears and defects after bombardment. This damage is most likely coupled with dangling bond rearrangement to lower the surface energy of the graphene through emission of low velocity carbon clusters.

7. CONCLUSIONS

The objective of the present research was the chemical characterization of nanodomains using massive cluster bombardment. A variety of samples were used to study the effects of confined nanodomains on the emission of secondary ions. Ion emission mechanisms for powders, nanoparticles, and 2D materials differ, but all allow for the characterization of chemical environments through the use of the event-by-event bombardment/detection technique.

First, the surface coverage of a CTAB surfactant on gold nanowires was calculated using an Au_{400} cluster probe. While no removal of this surfactant layer was observed by SIMS, the ability to select sub ensembles using coincidental methodology was demonstrated. The surface density of nanoparticles on a support was calculated to be $\sim$50%, and from the same experimental measurement it is possible to select sub ensembles that allow to calculate the coating coverage. The coverage of the gold nanowire is on a micron scale as the wire is < 100 nm by 5 μm. The surface ligand coverage of the CTAB, however, is on the nanoscale and nearly complete ($\sim$90%). Thus, through the selection of characteristic peaks it is possible to inspect the chemical environment at two different resolutions. Both measurements are spatially limited to a resolution of the emission volume ($\sim$10 nm) but are observed over two size regimes.

In order to probe the limit of spatial resolution, ultra small gold nanoparticles encapsulated within a dendrimer structure were studied. With as few as 55 gold atoms per nanoparticle, the ultimate detection sensitivity of the Au_{400} instrument was tested. Here, not only is secondary ion signal observed from all sizes of the available nanoparticles, but yields increase linearly with increasing size. This linearity

suggests that the size of the nanoparticle does not influence the ionization probability of the emitted gold ions as each impact fully atomizes the nanoparticle.

Interestingly, a preference for nanoparticle growth in regions of undamaged dendrimer structure. When the dendrimer branches undergo reductive damage, the nanoparticle segregates itself during growth. The amount of reductive damage is shown to be proportional to the degree of segregation between the two. This allows for the possibility to direct the growth of nanoparticles within support systems to selected sites rather than in an uniform, stochastic manner.

The recombination products and mechanism between a carbonaceous impactor (C_{60}) and inorganic powder targets was also studied. The use of the coincidental methodology allows for the selection of impacts only on the sample surface and not on the support structure, ensuring that only sample-projectile interactions are used for analysis. The effect of projectile velocity is observed as yields increase with final impact velocity.

The use of isotope labeling allows for the determination of zones of production for biologically relevant recombination ions. First, the use of a labeled projectile allows to determine the source of carbon as either delivered by the projectile or from contamination on the surface. By monitoring the yield of a projectile-surface recombination peak, such as $^{13}C^{15}N^-$, it is observed that an increase in impact velocity decreases the yield. The must mean that the projectile is burying itself in the sample surface and limiting the amount of labeled carbon available for reemission. More complicated 3 body recombinations do not show either an increase or decrease in yield with impact energy. Here, the recombination is limited by the amount of delivered carbon and the probability of atomic interaction between three atoms. Future studies should focus on the addition of position sensitive detectors so that radial velocities can be determined. This additional information could allow for

the determination of recombination and emission mechanisms during the projectile-sample interaction.

Finally, ion emission from a true confined volume was studied by bombarding 2D graphene targets. Detection in the transmission and reflection directions allow for the study of emitted secondary ions. Four emission processes are hypothesized, each with characteristic ions emitted. A direct interaction between the graphene and projectile results in small carbon clusters in the transmission direction. The excited rim around the hole produces high velocity secondary ions and a high charge state on this rim causes hydrogen cluster and C^+ emission in both directions. Finally, propagation of tears and hole damage produce low velocity, negatively charged carbon clusters up to C_{12}^-.

A high percentage of carbon atoms in the impact zone are ionized when compared to bulk pyrolytic graphite. The increase in ionization probability has yet to be explained. The majority of emitted ions are detected in the transmission direction due to the correlated momentum pulse from the projectile. Different graphene layer thicknesses show little to no effect on the ion emission, and the holes produced during bombardment are substantially larger than the impacting projectiles. This suggests a new process of ion emission. In the future, an investigation of the emitted secondary ion radial velocities would add important information to the ionization and emission mechanisms.

Further work should focus on the expansion of massive cluster SIMS as a tool to probe chemical nanodomains. While this work has presented clusters up to Au_{400}^{4+}, gold clusters of Au_{2800}^{7+} have been produced and can be applied to similar analytical investigations. A question that remains to be answered is the limit of cluster size where increasing fragmentation outpaces molecular ion emission.

The studies presented have shown that ultra small nanoparticles up to bulk pow-

der samples can all be analyzed using this powerful technique. Coincidental analysis allows to study preferential colocation within a sample, which leads to important information about directing synthesis and growth in targeted areas. True single nanoparticle analysis allows for the separation of subensembles, and using the size dependence of secondary ion production could allow for the study of mixed nanoparticle analysis where chemical information can identify the nanoparticle type and ion yields can inform nanoparticle size.

REFERENCES

[1] P. Williams. *Annu. Rev. Mater. Sci.*, 15:517–548, 1985.

[2] A. Benninghoven. *Phys Status Solidi*, 34:K169, 1969.

[3] V. Bernard. *Phys. Scripta*, 60, 1997.

[4] H. H. Andersen, A. Brunelle, S. Della-Negra, J. Depauw, D. Jacquet, and et al. *Phys. Rev. Lett.*, 80:5433–5436, 1998.

[5] P. Sigmund. *Nucl. Instrum. Meth. B*, 27:1–20, 1987.

[6] F. Gronlund and W. J. Moore. *J. Chem. Phys.*, 32:1540, 1960.

[7] P. K. Rol, J. M. Fluit, and J. Kistemaker. *Physica*, 26:1000, 1960.

[8] A. Wucher. *Appl. Surf. Sci.*, 252:6482, 2006.

[9] A. D. Appelhans and J. E. Delmore. *Anal. Chem.*, 61:1087, 1989.

[10] M. G. Blain, S. Della-Negra, H. Joret, Y. Le Beyec, and E. A. Schweikert.

[11] M. J. VanStipdonk, R. D. Harris, and E. A. Schweikert. *Rapid Commun. Mass Sp.*, 10:1987, 1996.

[12] S. C. C. Wong, R. Hill, P. Blenkinsopp, N. P. Lockyer, D. E. Weibel, and J. C. Vickerman. *Appl. Surf. Sci.*, 203:219, 2003.

[13] D. Weibel, S. Wong, N. Lockyer, P. Blenkinsopp, R. Hill, and J. C. Vickerman. *Anal. Chem.*, 75:1754, 2003.

[14] M. Benguerba, A. Brunelle, S. Della-Negra, J. Depauw, H. Joret, and et al. *Nucl. Instrum. Meth. B*, 62:8–22, 1991.

[15] A. Tempez, J. A. Schultz, S. Della-Negra, J. Depauw, D. Jacquet, A. Novikov, Y. Lebeyec, M. Pautrat, M. Caroff, M. Ugarov, H. Bensaoula, M. Gonin, K. Fuhrer, and A. Woods. *Rapid Commun. Mass Sp.*, 18:371, 2004.

[16] J. D. Debord. *Ph.D. Dissertation, Texas A&M University*, College Station, TX:Evaluation of Hypervelocity Gold Nanoparticles for Nanovolume Surface Mass Spectrometry, 2013.

[17] S. Della-Negra, J. Arianer, J. Depauw, S. V. Verkhoturov, and E. A. Schweikert. *Surf. Interface Anal.*, 43:66, 2011.

[18] S. Bouneau, S. Della-Negra, J. Depauw, D. Jacquet, Y. Le Beyec, J. P. Mouffron, A. Novikov, and M. Pautrat. *Nucl. Instrum. Meth. B*, 225:579, 2004.

[19] A. Brunelle, S. Della-Negra, J. Depauw, H. Joret, and Y. Lebeyec. *Rapid Commun. Mass Sp.*, 5:40, 1991.

[20] M. J. Eller. *Ph.D. Dissertation, Texas A&M University*, College Station, TX:Surface mapping based on the correlated emission of ions and electrons from hypervelocity C60 impacts, 2013.

[21] S. R. Rajagopalachary. *Ph.D. Dissertation, Texas A&M University*, College Station, TX:Characterization of Individual Nanoparticles and Applications of Nanoparticles in Mass Spectrometry, 2010.

[22] Z. Li, S. V. Verkhoturov, and E. A. Schweikert. *Anal. Chem.*, 78:7410, 2006.

[23] Z. Li, S. V. Verkhoturov, J. E. Locklear, and E. A. Schweikert. *Int. J. Mass Spectrom.*, 269:112, 2008.

[24] D. K. Smith and B. A. Korgel. *Langmuir*, 24:644–649, 2008.

[25] A. L. Liopo, S. Wang, P. J. Derry, A. A. Oraevsky, and E. R. Zubarev. *RSC Adv.*, 5:91587, 2015.

[26] L. Vigderman, P. Manna, and E. R. Zubarev. *Angew. Chem. Int. Ed.*, 51:636–641, 2012.

[27] E. Martinsson, M. M. Shahjamali, N. Large, N. Zaraee, Y. Zhou, G. C. Schats, C. A. Mirkin, and A. Daniel. *Small*, 12:330–342, 2016.

[28] N. Chanda, R. Shukla, K. V. Katti, and R. Kannan. *Nano Lett.*, 9:1798–1805, 2009.

[29] P. P. Joshi, S. J. Yoon, W. G. Hardin, S. Emelianov, and K. V. Sokolov. *Bioconjugate Chem.*, 24:878, 2013.

[30] H. J. Parab, H. M. Chen, T. C. Lai, J. H. Huang, P. H. Chen, R. S. Liu, M. Hsiao, C. H. Chen, and D. P. Tsai. *J. Phys. Chem. C*, 113:7574–7578, 2009.

[31] M. J. A. Hore, X. Ye, J. Ford, Y. Gao, J. Fei, Q. Wu, S. J. Rowan, R. J. Composto, C. B. Murray, and B. Hammouda. *Nano Lett.*, 15:5730–5738, 2015.

[32] C. K. Liang, S. V. Verkhoturov, L. J. Chen, and E. A. Schweikert. *Int. J. Mass Spectrom.*, 334:43, 2013.

[33] R. M. Crooks, M. Zhao, L. Sun, V. Chechik, and L. K. Yeung. *Acc. Chem. Res.*, 34:181, 2001.

[34] M. Zhao and R. M. Crooks. *Angew. Chem. Int. Ed.*, 38:364, 1999.

[35] M. Zhao and R. M. Crooks. *Adv. Mater.*, 11:217, 1999.

[36] F. A. Fernandez-Lima, J. D. DeBord, M. J. Eller, S. V. Verkhoturov, S. Della-Negra, A. S. Woods, and E. A. Schweikert. *Anal. Chem.*, 83:8448, 2011.

[37] M. E. Garcia, L. A. Baker, and R. M. Crooks. *Anal. Chem.*, 71:256, 1999.

[38] A. B. Clubb, M. J. Eller, S. V. Verkhoturov, E. A. Schweikert, R. M. Anderson, and R. M. Crooks. *J. Vac. Sci. Technol. B.*, 114:03H104, 2016.

[39] N. Winograd, Z. Postawa, J. Cheng, C. Szakal, J. Kozole, and B. Garrison. *Appl. Surf. Sci.*, 252:6836–6843, 2006.

[40] D. Gross and G. Grodsky. *JACS*, 77:1678–1680, 1955.

[41] C. Guillermier, S. Della-Negra, E. A. Schweikert, A. Dunlop, and G. Rizza. *Int. J. Mass Spectrom.*, 275:86–90, 2008.

[42] M. Sachse, J. Schmidt, S. Kempf, and F. Spahn. *J. Geophys. Res. Planets.*, 120:1847–1858, 2015.

[43] Y. Morita, K. Nakajima, M. Suzuki, K. Narumi, Y. Saitoh, W. Vandervorst, and K. Kimura. *Nuc. Instr. and Meth. B*, 269:2080–2083, 2011.

[44] J. D. Carpenter, T. J. Stevenson, G. W. Fraser, J. C. Bridges, A. T. Kearsley, R. J. Chater, and S. V. Hainsworth. *J. Geophys. Res. Planets.*, 112, 2007.

[45] S. M. M. Ramos, N. Bonardi, B. Canut, and S. Della-Negra. *Phys. Rev. B*, 57:189, 1998.

[46] A. Colder, B. Canut, M. Levalois, P. Marie, X. Portier, and S. M. M. Ramos. *J. Appl. Phys.*, 91:5853, 2002.

[47] F. R. F. Fan and A. J. Bard. *Nano Lett.*, 8:1746, 2008.

[48] A. Delcorte and B. J. Garrison. *Nucl. Instrum. Methods Phys. Res., Sect. B*, 303:179, 1990.

[49] M. A. Park, K. A. Gibson, L. Quinones, and E. A. Schweikert. *Science*, 248:988, 1990.

[50] O. Lehtinen, J. Kotakoski, A. V. Krasheninnikov, A. Tolvanen, K. Nordlund, and J. Keinonen. *Phys. Rev. B*, 81:153401, 2001.

[51] T. H. Fang, T. Wang, J. C. Yang, and Y. J. Hsiao. *Nanoscale Res. Lett.*, 6:481, 2011.

[52] W. Wang, S. Li, J. Min, C. Yi, Y. Zhan, and M. Li. *Nanoscale Res. Lett.*, 9:41, 2014.

[53] X. Y. Liu, F. C. Wang, H. S. Park, and H. A. Wu. *J. Appl. Phys.*, 114:054313, 2013.

[54] S. Liu, Q. Zhao, J. Xu, K. Yan, H. Peng, F. Yang, L. You, and D. Yu. *Nanotechnology*, 23:085301, 2012.

[55] S. Zhao, J. Xue, L. Liang, Y. Wang, and S. Yan. *J. Phys. Chem. C*, 116:11776, 2012.

[56] A. Delcorte, B. J. Garrison, and K. Hamraoui. *Anal. Chem.*, 81:6676, 2009.

[57] J. D. Debord, S. Della-Negra, F. A. Fernandez-Lima, S. V. Verkhoturov, and E. A. Schweikert. *J. Phys. Chem. C*, 116:8138, 2012.

[58] A. C. Ferrari, J. C. Meyer, V. Scardaci, C. Casiraghi, M. Lazzeri, F. Mauri, S. Piscanec, D. Jiang, K. S. Novoselov, S. Roth, and A. K. Geim. *Phys. Rev. Lett.*, 97:187401, 2006.

[59] H. Feld, R. Zurmuehlen, A. Leute, and A. Benninghoven. *J. Phys. Chem.*, 94:4595, 1990.

[60] J. D. DeBord, S. Della-Negra, F. A. Fernandez-Lima, S. V. Verkhoturov, and E. A. Schweikert. *J. Phys. Chem. C*, 116:8138–8144, 2012.

[61] H. Feld, R. Zurmuehlen, A. Leute, and A. Benninghoven. *J. Phys. Chem.*, 94:4595–4599, 1990.

[62] C. W. Diehnelt, M. J. Van Stipdonk, and E. A. Schweikert. *Phys. Rev. A: At. Mol. Opt. Phys.*, 59:4470–4474, 1999.

[63] H. Gnaser. *Nucl. Instrum. Methods Phys. Res., Sect. B*, 149:38–52, 1999.

[64] W. Guthier, O. Becker, S. Della-Negra, W. Knippelberg, Y. Le. Beyec, U. Weikert, K. Wien, P. Wieser, and R. Wurster. *Int. J. Mass Spectrom. Ion Phys.*, 53:185, 1983.

[65] F. A. Fernandez-Lima, C. R. Ponciano, E. F. da Silveira, and M. A. C. Nascimento. *Chem. Phys. Lett.*, 445:147–151, 2007.

[66] M. Most, K. Wien, A. Brunelle, S. Della-Negra, J. Depauw, D. Jacquet, M. Pautrat, and Y. LeBeyec. *Nucl. Instrum. Methods Phys. Res., Sect. B*, 168:203, 2000.

[67] K. Wien, O. Becker, and W. Guthier. *Radiat. Eff.*, 99:267, 1986.

[68] J. F. Ziegler, J. P. Biersack, and U. Littmark. *The Stopping and Range of Ions in Solids*, Pergamon, 1985.

[69] K. Kim, V. I. Artyukhov, W. Regan, Y. Liu, M. F. Crommie, B. I. Yakobson, and A. Zettl. *Nano Lett.*, 12:293, 2011.

[70] P. Koskinen, S. Malola, and H. Hkkinen. *Phys. Rev. Lett.*, 101:115502, 2008.

APPENDIX A

REVISED SOURCE PREPARATION PROCEDURE

Etching Solution Preparation:

1. Prepare an aqueous solution of 35% w/w NaOH in a plastic bottle. Write the date prepared on the container (solutions should be made fresh every 3 months).

2. Mix 10 mL of 35% NaOH solution, 50 mL of glycerol, and 50 mL of distilled water in a beaker and stir.

3. Etching solution should be made the day of etching or oxide coating will be incompletely removed.

Needle Preparation:

1. Cut a section of tungsten wire (0.200 mm diameter) approximately 5 cm long. Clean with automotive grade sandpaper (600 grit). The mechanical removal of the oxide layer needs to be done the same day as assembling and dipping the source, so do not prepare needles in bulk and store.

2. Place wire in pin vice and center. Pull the wire from the base of the pin vice to the tip in order to straighten the wire.

3. Cut wire to a length of 3 cm.

4. Etch the needle using the following procedure:

a. Place the needle pin vice into the Teflon needle brace, and place the needle brace in the Teflon block.

b. Use the course adjustment on the platform to bring the solution to the needle. Use the find adjustment on the stand to make the final positional adjustments.

c. The end of the wire may be split as a result of the cutting. This potion must be

removed before etching the needle, either by re-cutting or by etching the bad portion off. Attach electrical connections and insert ∼1 mm of the needle into the solution and apply AC voltage until bubbles begin to form on the tungsten surface.

d. Pull the needle up so that a minimal amount of the needle is in the solution but still retains the meniscus of etching solution. Etch until the needle cone has a half angle of 49.5^o.

e. After the point is etched, submerge the needle 15 mm into the solution and etch to remove the oxide layer for 10 minutes. Rinse with distilled water.

Spring Reservoir Preparation:

1. Cut ∼20 cm piece of tungsten wire (0.200 mm diameter) and clean with automotive grade sandpaper. Bend wire in all directions while cleaning in order to break the memory of the wire. Reservoirs should be made the day of source preparation so the mechanical removal of oxide layers is not lost.

2. Using the source winder, tape tungsten wire to top of the turner. Wind six turns, then remove tape and allow the leg to unwind from its tension. Remove screw and carefully remove reservoir.

3. Check shape using a magnifying glass. There should be no gaps in between turns and faces should be parallel.

4. Cut spring ends to proper length using the spring jig. Do not bend the legs. Insert legs into the source assembly and tighten screws gently. Over tightening will cause stress on the spring and may cause opening upon dipping.

5. Immerse spring into the etching solution and while etching use another piece of wire to remove air bubbles. Etch 10 minutes, then rinse with distilled water.

Inserting Needle into Spring Assembly:

1. Accurately measure 20 mm from the tip of the needle and cut off excess.

2. Insert needle into the source assembly using tweezers to position the needle into the middle of the spring.

3. The reservoir should be centered in the side view of the spring, and must be in a vertical position above the spring at a right angle to the top of the spring. Use millimeter paper to adjust the height of the needle to 1.3 mm above the spring.

4. Tighten the screw of the needle pin vice gently. Introducing tension may cause the needle to shift during dipping.

5. Dip the entire assembly into the etching solution for 10 minutes. When all of the oxide layer is removed the color after rinsing with distilled water will be dark grey and matte in finish.

Inserting Source Assembly into Vacuum:

1. Attach the source assembly to the vertical translator and attach wires to feedthrough. Check connection using multimeter.

2. Au/Si eutectic (97% Au, 3% Si Academy Precision Metals) should already be in tantalum boat in vacuum chamber. If it needs replacing, 3/8 rod should be cut and sonicated in ethanol.

3. Clean chamber and boat with ethanol, then pump down to at least $1\mathrm{x}10^{-6}$ Torr.

4. Heat eutectic in steps until melted. Increase 5% every 5 minutes until power supply is at 35% power. Eutectic melts at 363°C. Check for melting by hitting chamber and watching for ripples.

5. Using a variac and transformer, heat one leg and needle until a dull red glow for 2 minutes. Repeat for the other leg and needle, and again for both legs. This fixes the shape of the source.

6. Heat again to a yellow-white glow in all three positions for 2 minutes each. This removes the oxide layer.

7. Heat between the two legs to a dull red and lower slowly into the eutectic. Turn off power and raise slowly at a constant rate.

8. Repeat last step until the source wets and fills completely.

9. Examine needle for the presence of a meniscus at the base going into the spring, and for full filling of the reservoir.

10. Turn off heating to boat in one step and wait until it is at room temperature before breaking vacuum.

APPENDIX B

ORGANIC-FREE CLEANING OF SAMPLE HOLDERS

Organic-Free Cleaning Procedure:

1. Scrub with Alconox soap solution.

2. Rinse with copious amounts of tap water followed by several rinses with MilliQ deionized water.

3. Triple rinse with hexane.

4. Triple rinse with acetone.

5. Triple rinse with dicholormethane.

6. Triple rinse with 1:1 volume solution of dichloromethane and methanol.

7. Triple rinse with methanol.

8. Tent with organically clean aluminum foil and dry overnight in 100° C oven.

Notes: All solvents must be at least HPLC grade.

It is best to clean a glass evaporating dish and the tenting foil a day before so that you have a clean place to hold and transport the powder holders/utensils you are preparing.

APPENDIX C

YIELD TABLE FOR $^{13}C_{60}$ BOMBARDMENT ON NH_4NO_3

Table C.1: Coincidental Percent Yields From Isotope Labeled Ammonium Nitrate at Different Impact Velocities of $^{13}C_{60}$. Estimated Error Approximately 10%.

Sample	$^{15}NH_4NO_3$				$NH_4^{15}NO_3$			
Energy (keV)	20	25	40	50	20	25	40	50
Velocity (km/s)	70	79	99	111	70	79	99	111
CN^-	1.4	2.1	2.7	3.4	1.4	2.0	2.7	3.4
$^{13}CN^-/C^{15}N^-$	1.4	2.0	2.4	3.1	1.4	2.0	2.4	3.1
$^{13}C^{15}N^-CNO^-$	0.16	0.15	0.13	0.11	0.16	0.15	0.13	0.11
$^{13}CNO^-/C^{15}NO^-$	0.38	0.41	0.52	0.66	0.37	0.41	0.52	0.66
$^{13}C^{15}NO^-$	0.069	0.075	0.059	0.075	0.069	0.075	0.056	0.075
NO_2^-	0.34	0.47	0.80	1.5	0.31	0.43	0.96	1.27